5.1 Introduction

The 7xxx series Al-alloys conform to the needs of aviation industries owing to improved specific strength, as well as those of creep and fatigue behaviors [16,21,90,126,231,232]. They are also suitable for ballistic [167], and electrical/thermal applications [233]. Properties required for such applications are met by suitable modifications of alloy chemistry and microstructures [154,234]. One of the ways to enhance specific strength refers to the precipitation hardening mechanisms for 7xxx series alloys [20]. Grain refinement of the matrix does affect the hardening process but significant strengthening in them is attained by the nature of coherency between the matrix and precipitates [183]. Therefore, less attention has been paid to refining the matrix in age-hardenable alloys. One of the variants of severe plastic deformation in combination with age-hardening techniques has been employed for improving the mechanical properties of Al-alloys [235]. Recently developed friction stir processing (FSP) has been advocated to be such a variant [14]. FSP affects the surface chemistry and microstructures along the transverse direction- nugget zone (NZ), thermo-mechanically affected zone (TMAZ), heat affected zone (HAZ), and base metal (BM) due to the rotational motion of a tool in external contact with specimen surface. Such a process may also alter the chemistry and microstructures along the longitudinal direction (depth-wise: top, middle, and bottom) due to internal contact-assisted mechanical stirring between the tool and the workpiece [14,22,137]. Owing to low metal loss and energy, FSP offers a relatively environmentally friendly processing route [14,22]. A common feature between friction stir welding and processing is that the tool is non-consumable [14,22]. Welding is employed for the coalescence or joining [23,236,237]. FSP, in contrast, refers to a technique to alter the microstructures and, at the same time lead to the formation of new phases [238,239]. As a consequence, FSP developed by the Welding Institute, U.K. (1991) has been

utilized for (i) achieving ultrafine grains [23], (ii) attaining the compositional and microstructural homogeneity [137,240], and (iii) giving impetus to various others beneficial effects. They refer to surface hardening [241], the fabrication of a hybrid, and in-situ surface [240]. This technique may also help in the synthesis of metal-matrix composites as well as for many other purposes [242–244], e.g., repairing components [240,245] and additive manufacturing [246]. Microstructural evolution from the previous studies shows dynamically re-crystallized grain (DRX) in the NZ, slightly elongated grains in TMAZ, and coarse-grain structures, in HAZ [22,107,137]. The structural and micro-structural in-homogeneities throughout the processed zone significantly affect the mechanical performances of the alloy system [137]. The evolution of complex dislocation structures also occurs in the nugget zone after FSP due to severe plastic deformation [95,96,126]. They refer to tangled dislocation, the wavy array of dislocation, dense dislocation walls (DDWs~), dislocation cell (D.C.), Taylor lattice, etc. [96,193,247]. Such a structural evolution strongly impacts mechanical performances and material flow behavior. AA7075T7352 is an alloy of the 7xxx series, which has been designated to obtain a high hardening exponent (n) along with a high ultimate tensile strength to yield strength ratio *(UTS/ YS)* to achieve deformation without neck formation [90,126]. Flow curve behaviors of various heat-treated 7075 Al-alloys and Ni-based super-alloys are studied by fitting the different mathematical models [126,170,172–174,180,248]. The heat-treated Al-alloys (AA7075T651, AA7075, AA6061, AA2024) after FSP giving rise to microstructural changes, significantly influencing the mechanical performances, are widely reported [22,99,137,249,250]. However, a defect-free successful friction stir processing of AA7075T7352 alloy and related structure property co-relation seems to be lacking in the literature. This work, therefore, focuses on the friction stir processing of AA7075T7352. Further, the matrix grain refinement, precipitation, and

dissolution in the alloy matrix by FSP are studied. The complex dislocation structure evolution, residual-stress analysis, and their impact on mechanical performances are explored. Various structural and microstructural characterization tools are employed to arrive at structure-property correlation. Micro-texture features are also studied with the help of electron backscattered diffraction (EBSD) data. This alloy series has many exciting precipitation sequences owing to the ratio of Zn/Mg. They refer to supersaturated solid solution (SSSS, α) → GP zones →η' →η, for Zn/Mg ratio (>2) [48,68,251]. Whereas, with a lower Zn/Mg ratio, the precipitation process changes its path, including the formation of a new phase (T-phase) [182], given as: Supersaturated solid solution (SSSS, α) → GP zones n→T' or η' →T or η. The GP zone is the coherent precipitate [122], whereas η' and η are semi-coherent and in-coherent by nature [122,151]. They show the formation of variants. For example, the GP zone has two variants (GP-I and GP-II) [68,74], whereas η' and η display 13 and 4 variants, respectively [68,74]. Due to FSP-assisted stirring, the majority of the transition (GP zones, η') and equilibrium (η) precipitates are reported to be broken into pieces and fragmented [33]. Moreover, friction stir-assisted thermal effect and dislocation environment change the size and chemistry of fragmented precipitates [11, 34]. For example, two reverse trends dissolution and re-precipitation are observed in the nugget zone [39-42]. Liu et al. [138] and Su et al. [137] reported coarsening/ evolution of the new precipitates. Whereas Sato et al. [139], Heinz et al. [104], and Jata et al. [140] noticed the dissolution of the phases. Therefore, such changes in the microstructures and chemistry after FSP may significantly change the precipitation process, thereby mechanical, chemical, and physical performances that are hardly reported in the literature. This is the motivation of the current work.

5.2 Results

5.2.1 Optical micrograph

Fig. 5.1a shows optical images of the as-received specimen (AR). It shows a dark contrast of the precipitates dispersed in the α-Al matrix, and the region with bright contrast is more than the dark one. Fig. 5.1b displays an optical micrograph of the interface. Separate areas of the nugget zone, heat-affected zone (affected by the heat and no plastic deformation), thermo-mechanically affected zone (affected by both heat and plastic deformation), and base-metal are seen. Fig. 5.1c depicts the microstructure of the nugget zone, which displays the grain refinement, shoulder marks, and undissolved precipitates. A similar microstructural gradient was also observed in the 2 passes, and 3 pass FSP with slightly changing the matrix grain in the nugget, TMAZ, and HAZ, which is further investigated with the help of microtexture characterization in EBSD. The optical images of 2-pass and 3-passes of FSP also display a similar microstructural gradient. Therefore, they are not shown separately.

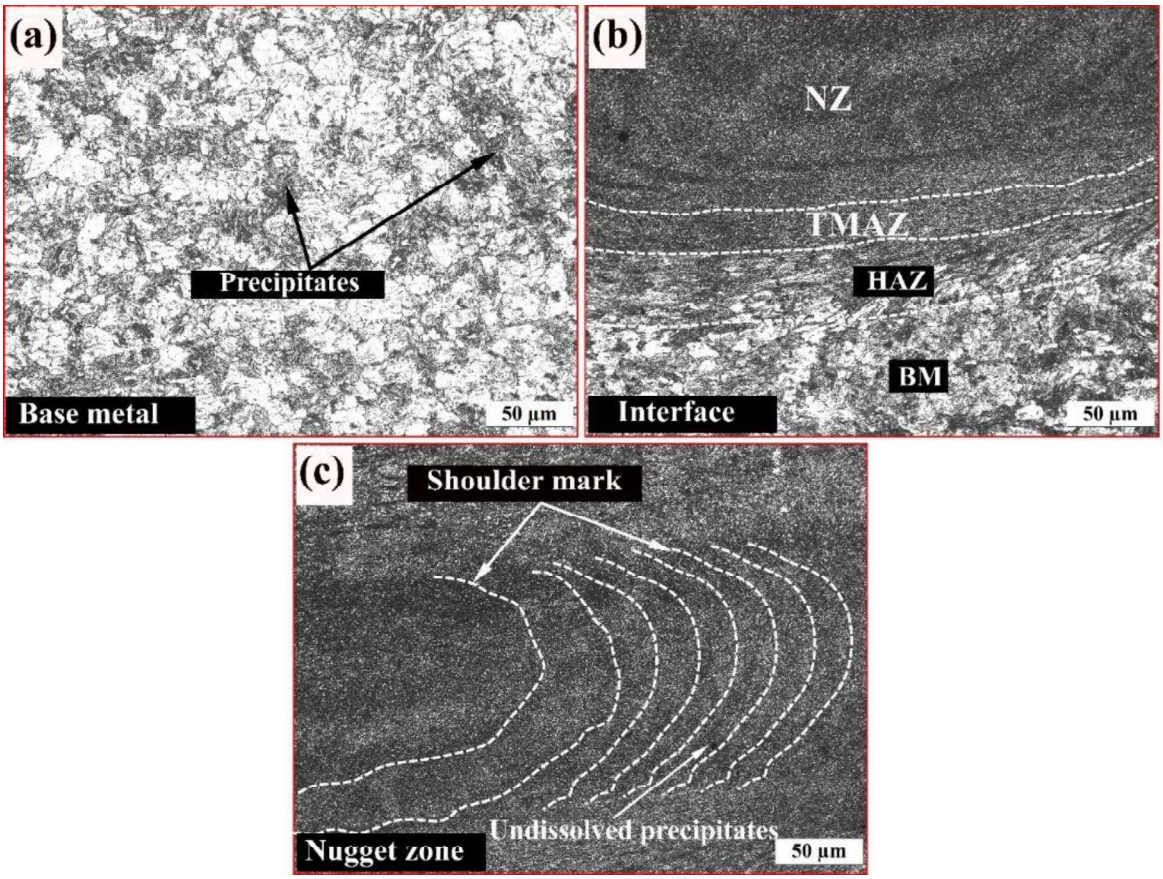

Figs. 5.1a-c Optical microstructure after FSP : (a) base-metal (R.S.), (b) Interface, consisting of the N.Z., HAZ, and base-metal, and (c) nugget-zone.

5.2.2 XRD and DTA analysis

Fig. 5.2a displays the x-ray diffraction (XRD) patterns of as-received AA7075T7352 alloy. A sharp crystalline peak of the α-Al, f.c.c. (P.S.= cF_4, Lattice parameter a= 4.08Å, space group=$Fm\bar{3}m$) are observed corresponding to the d-spacing values of 2.33 Å, 2.03Å, 1.43Å, and 1.21Å. Low-intensity XRD peaks of η, η' and η (Laves phase of C14 type, AB_2 structures, lattice parameter, a =5.23Å), and intermetallic of Al_2Cu are noticed respectively to the d-spacing value of 4.29Å, 2.13°, and 2.15Å. Fig. 5.2b shows the XRD pattern after 1-pass FSP. A sharp crystalline peak of α-Al is also noticed with changes in the preferred crystal orientation from 111 of α-Al to 200 of α-Al. The d-spacing values are slightly changed as the peak position slightly shifted towards the right from their original position in the as-

received state. Low-intensity peak is found absent at a d-spacing value of 4.29Å. Other two minor peaks are observed corresponding to the d-spacing value of 2.10Å, and 1.87Å. Further, appearances of the new peak are observed respectively to the d-spacing value of 2.49Å. Fig. 5.2c portrays the XRD pattern, after 2-pass FSP (at 1000rpm). The absence of XRD peaks is noticed respectively to a d-spacing value of 2.33 Å, 2.01 Å, 1.43 Å and 1.21Å. Low-intensity peak at d=4.29Å is found absent, and the other two minor peaks are seen respective to d-spacing values of 2.11 and 1.87Å.

Fig. 5.2d depicts the XRD patterns after 3-pass FSP. Analyzed peaks also display the presence of sharp crystalline peaks of α-Al, with changes in preferred crystal orientation as 111 of α-Al, and the intensity of other peaks is gradually decreasing. The minor crystalline peak of the ηis noticed with slight changes in the d-spacing value of 4.23Å. Other less intense crystalline peaks of η' and η are also noticed by shifting their original peak position towards the right.

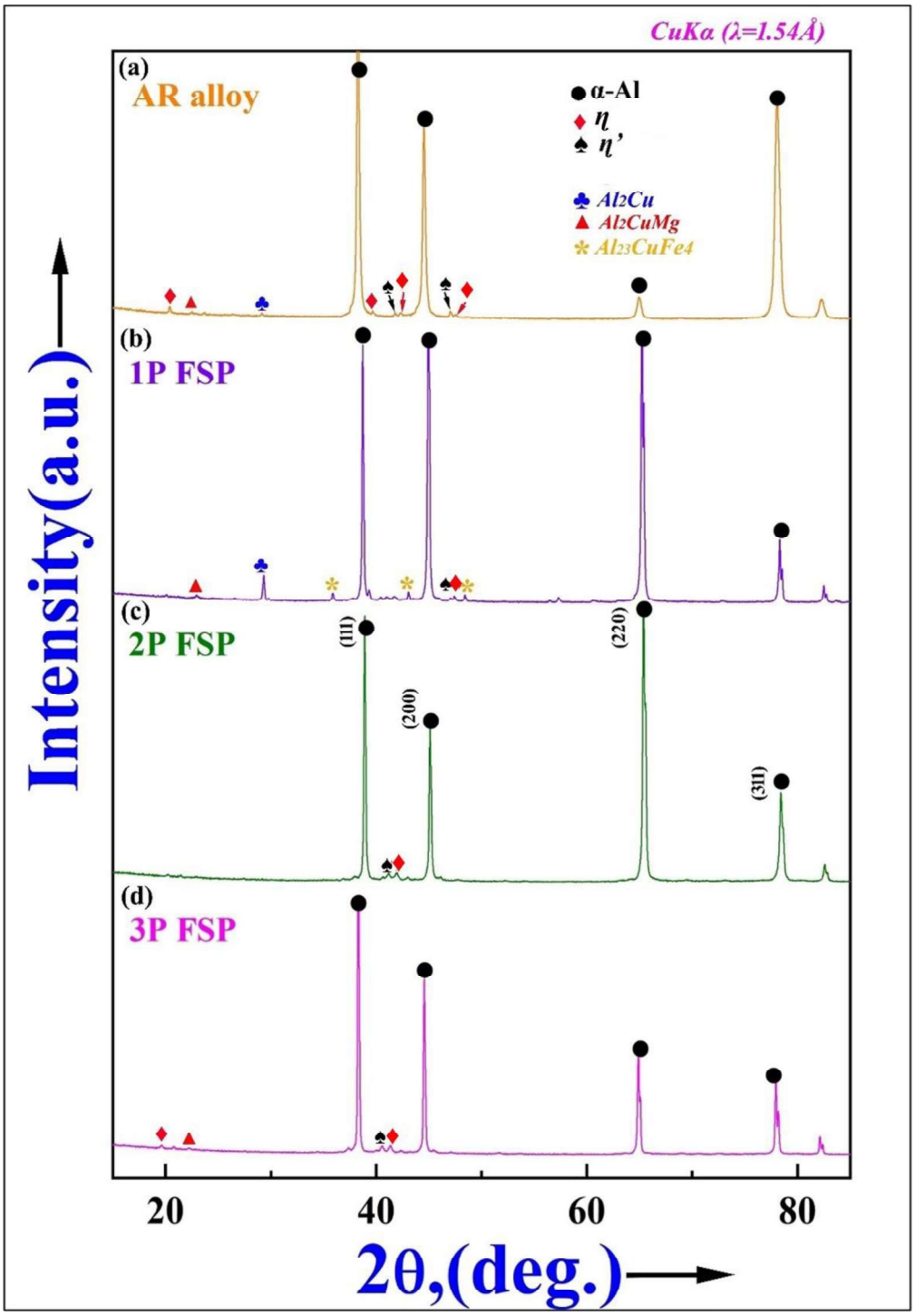

Figs. 5.2a-f XRD peaks of (a) as-received, (b) 1pass FSP, (c) 2pass FSP, and (d) 3pass FSP, (e) XRD peaks (111) of α-Al, after multi-pass FSP, in 2θ range of 38° to 39.5°, peaks in 1pass & 2pass FSP shifted toward right, but after 3pass FSP, peak was shifted to left, (f) DTA thermogram upto 773K from three different zones of NZ, HAZ and BM after FSP.

Fig. 5.2e shows the XRD peak, 111 of α-Al in 2θ range of 38° to 39.5°. The 111, reflection of AR alloy (base metal) is less intense. On the other hand, a slightly broad and right-shifted XRD peak is observed after 1 pass of FSP, supporting the dissolution of the η. In the 2-pass FSP, 111 peaks further shifted towards the right side supporting the dissolution of the ηand η' but the peak intensity of *η'* is less than the 1-pass FSP, showing the higher dissolution. After 3pass FSP, the 111 peak is shifted towards the left of the 111 peak of AR alloy. This supports the re-precipitation of the η.

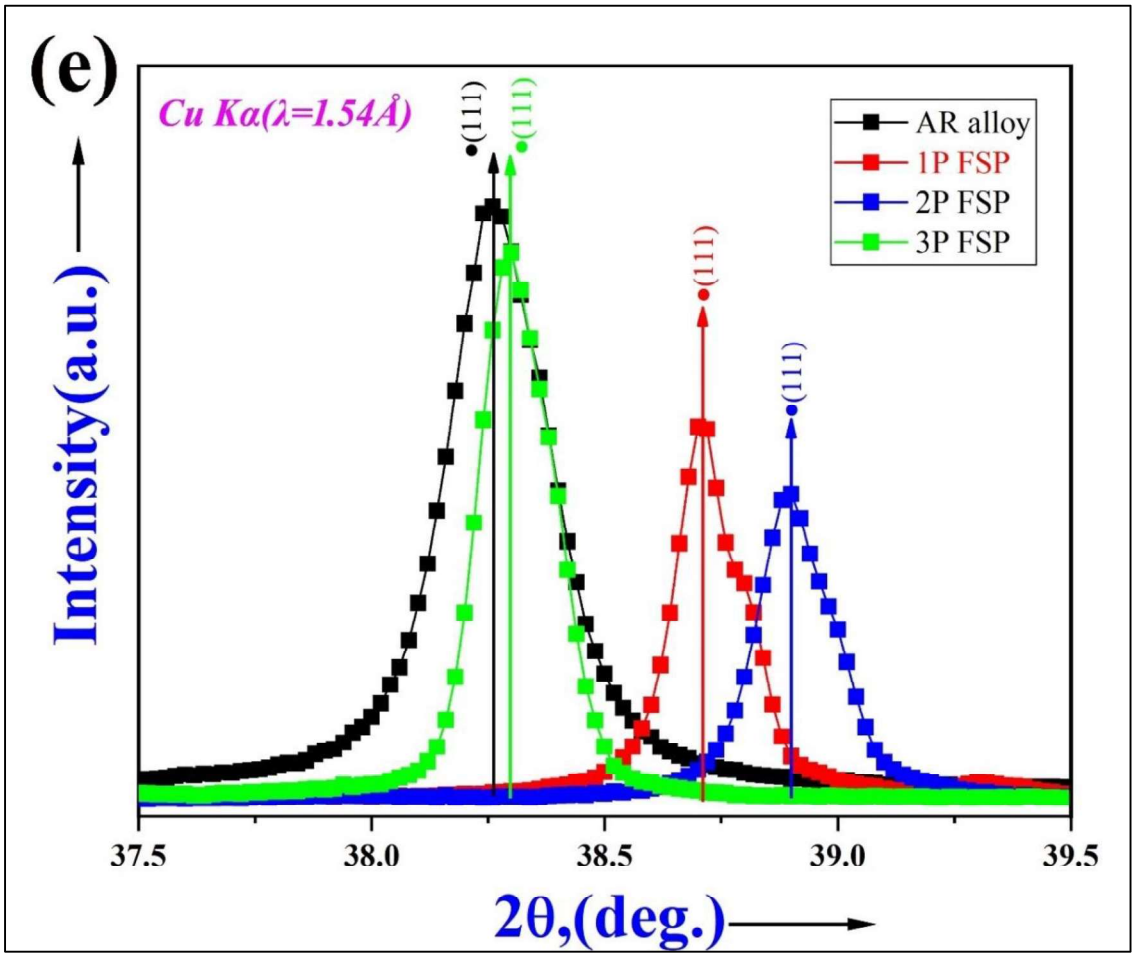

Fig. 5.2a-f Continued……..

The lattice micro-strain (ε), crystallite size (*D in Å*), and dislocation density of the AR alloy, and after FSP are calculated using the XRD data with the help of Liebenberg Marquardt least-square regression method, and their values are given in Table 5.1.

Table 5.1 Lattice micro-strain (ε), crystallite size (*D in Å*), and dislocation density

Processing state	**Lattice micro-strain** (ε_{av})	**Crystallite size** ***(D in Å)***	**Dislocation density** ($x10^{17}/m^2$)
AR alloy	0.21	3.8	144
1pass FSP	0.13	7.2	37
2pass FSP	0.10	10.1	25
3pass FSP	0.14	16.02	12

Fig. 5.2f shows DTA thermo-gram of AR alloy (base metal, BM), and after FSP (e.g., nugget zone and heat affected zone). The presence of three humps (positive peaks) is noticed respectively to the 523K, 663K, and 753K. After FSP, three negative peaks are observed corresponding to the same temperature showing the dissolution of phases. However, the peak in NZ is more negative than AR alloy. On the other hand, peaks in the HAZ, and NZ remain positive. The peaks in the DTA thermogram illustrate changes in the temperature, and shifting from the baseline.

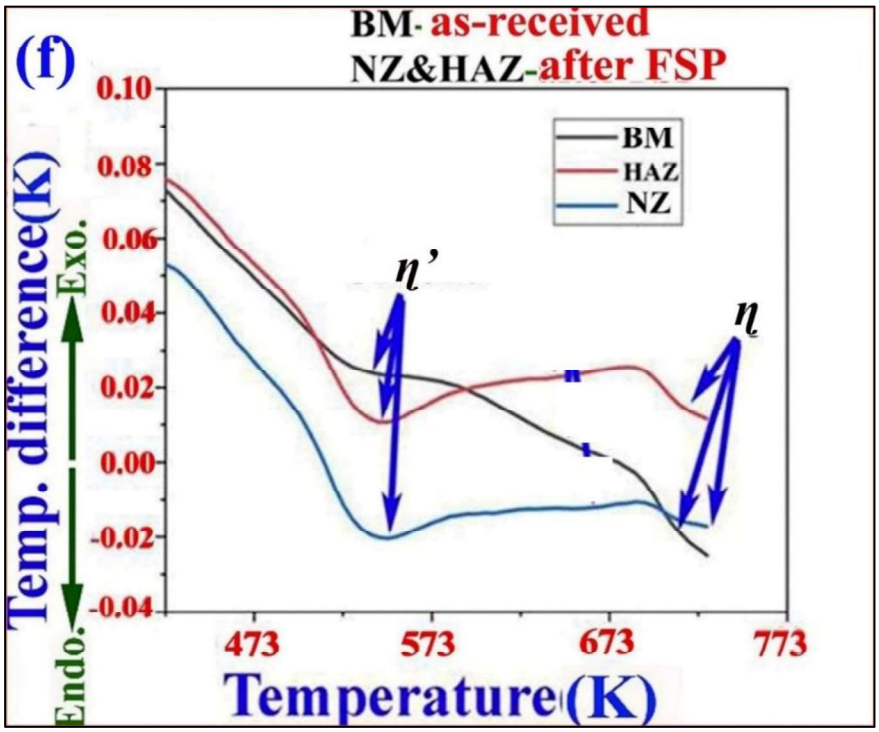

Figs. 5.2a-f Continued……

5.2.3 Microtexture

Fig. 5.3a displays ODF, Φ_2 = 0°, 45°, 65° sections of the AR alloy. Evolution of the Goss {011} <100> texture component of intensity 25.5 at Φ_2 = 0° of orientation 1, rotated P of orientation 2, rotated cube texture components of intensity range 7.6 to 24.5 at Φ_2 = 45° of orientations 5-8, and slightly rotated Bs texture component {011} <211> of intensity 8.2 at Φ_2 = 65° section of orientation 10, are observed. In addition to this, other texture components of orientations 2,3,4, 9, and 11 are also observed.

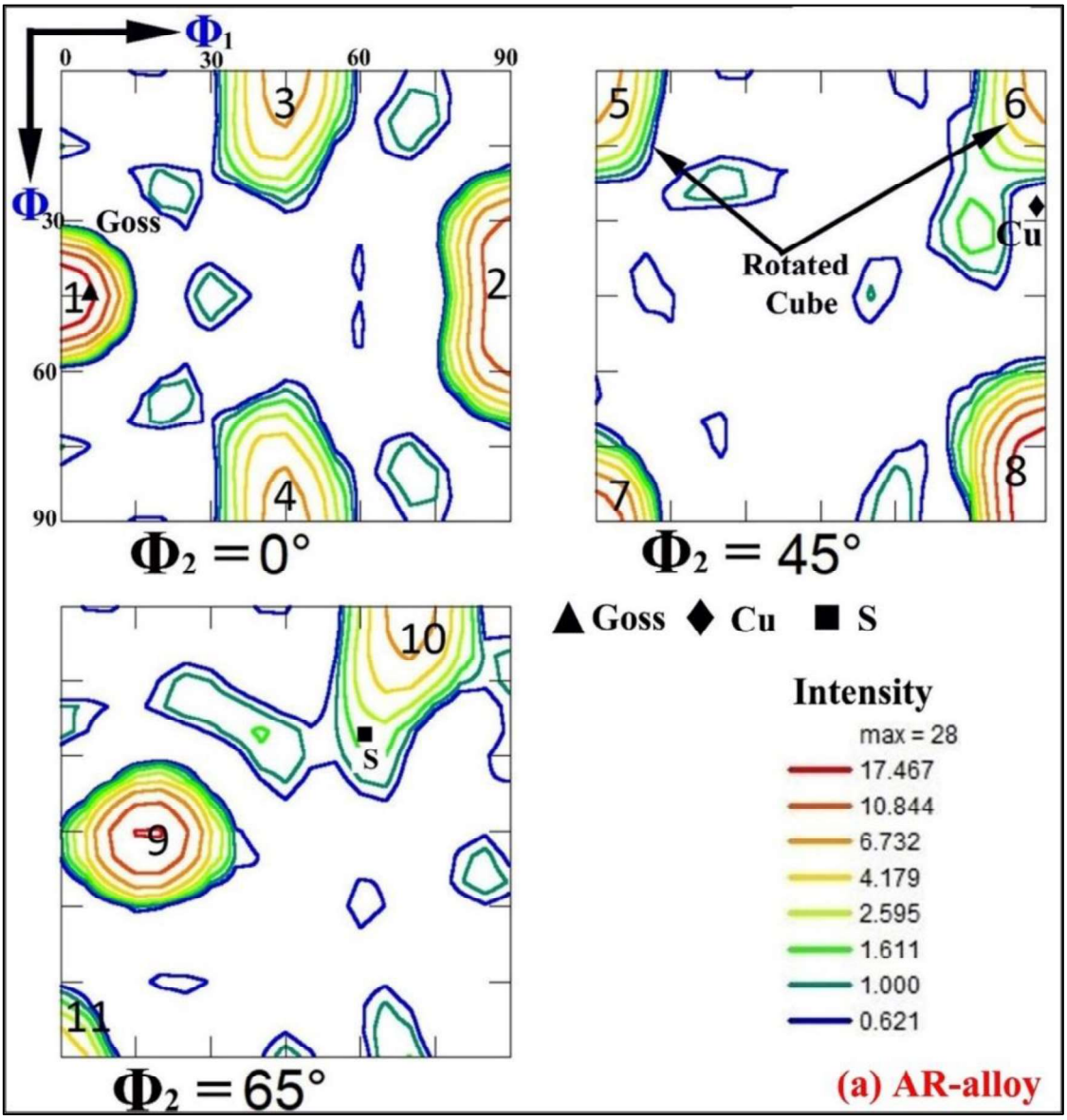

Figs. 5.3a-d orientation distribution function (ODF), Φ_2 = 0°, 45°, 65° sections of (a) base-metal, (b) 1pass FSP, (c) 2pass FSP, and (d) 3pass FSP.

The details of each texture component, its orientation, and its relative intensity are given in Table 5.2.

Table 5.2 Texture components, their orientation, and relative intensity in the AR state

Orientation No.	Texture components (h k l) [u v w]	Euler angles of orientation (Φ_1, Φ, Φ_2)	Intensity (x Random)
01	(1 1 1) [30 $\bar{1}$ 1]	1.6°, 44.8°, 0.0°	25.5
02	(0 1 1) [1 $\overline{15}$ 15]	88.0°, 43.2°, 0.0°	13.4
03	(0 1 18) [18 $\overline{18}$ 1]	44.4°, 2.0°, 0.0°	8.2
04	(0 14 1) [14 $\bar{1}$ 14]	44.4°, 86.8°, 0.0°	8.1
05	(0 1 22) [20 $\overline{22}$1]	2.4°, 2.4°, 45.0°	7.6
06	(1 1 23) [$\overline{11}$ $\overline{12}$1]	88°, 2.4°, 45.0°	7.6
07	(11 11 1) [1 $\bar{1}$ 0]	1.6°, 87.2°, 45.0°	12.2
08	(11 11 3) [$\overline{45}$ 33]	88°, 78.5°, 45.0°	24.5
09	(8 4 9) [4 $\overline{17}$4]	16.7°, 44.8°, 65.0°	17.6
10	(1 1 26) [$\overline{13}$ $\overline{13}$1]	69.4°, 2.8°, 65.0°	8.2
11	(13 6 1) [11 $\overline{24}$1]	4.2°, 86.8°, 65.0°	4.6

Fig. 5.3b shows, the ODF of Φ_2 = 0°, 45°, 65° sections of the NZ, after 1pass FSP. The reduced intensity of 2.1 of Goss {011} <100> texture in orientation 1, and rotated cube {013} <100> texture components of intensity range 1.5-2.5 in orientations 3-6 are found. The Bs {011} <211> texture component is rotated to orientation 9 at Φ_2=65° section, A few other texture components like orientation 2, 7-9 are also identified. It is observed that FSP randomizes the texture of the as-received alloy.

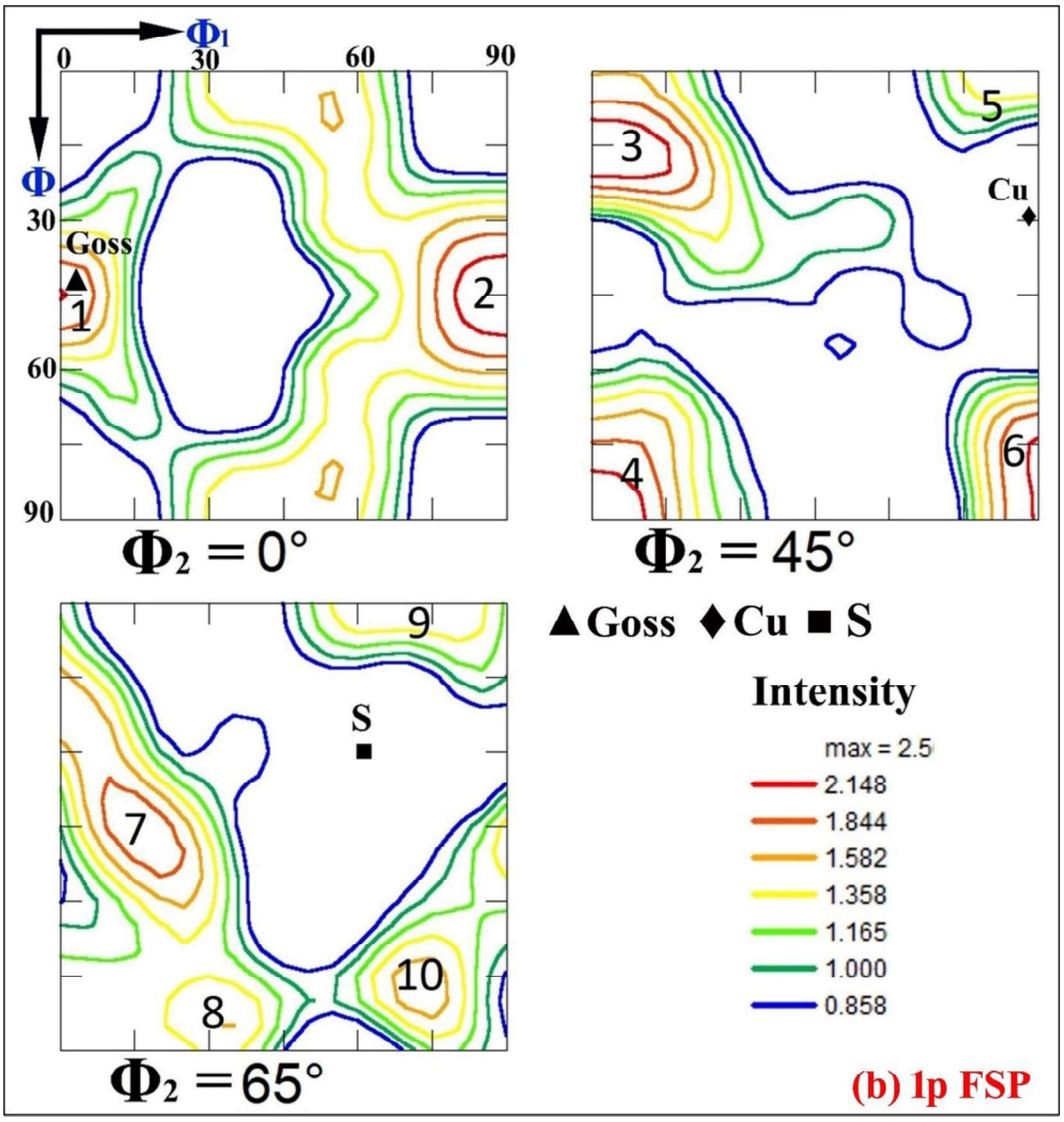

Figs. 5.3a-d Continued.....

The details of each texture component, its orientation, and its respective intensity are given in Table 5.3.

Table 5.3 Texture components, orientation, and relative intensity after 1 pass FSP

Orientation No.	Texture components (h k l) [u v w]	Euler angles of orientation (Φ_1, Φ, Φ_2)	Intensity (x Random)
01	(0 1 1) [1 0 0]	1.2°, 44.0°, 0.0°	2.1
02	(0 12 13) [1 $\overline{13}$ 12]	86.8°, 43.6°, 0.0°	2.4
03	(1 1 6) [32 $\overline{38}$ 1]	5.6°, 14.3°, 45.0°	2.5
04	(18 17 3) [14 $\overline{15}$ 1]	3.2°, 83.7°, 45.0°	2.3
05	(0 0 1) [$\overline{7}$ $\overline{9}$ 0]	82.9°, 2.0°, 45.0°	1.5
06	(1 1 23) [$\overline{11}$ $\overline{12}$ 1]	88.8°, 76.5°, 45.0°	2.2
07	(16 7 18) [3 $\overline{12}$ 2]	1.6°, 87.2°, 45.0°	2.1
08	(11 11 3) [$\overline{4}$ $\overline{5}$ 33]	30.9°, 82.1°, 65.0°	1.5
09	(0 0 1) [$\overline{1}$ $\overline{1}$ 0]	70.2°, 1.6°, 65.0°	1.5

Fig. 5.3c displays ODF, Φ_2 = 0°, 45°, 65° sections of NZ, after 2pass FSP. The texture intensity further decreases from 2.5 times random to 1.6 times random. The low intensity of 1.2 of Goss {011} <100> texture is observed in orientation number 0. A slightly higher intensity of 1.6 of other texture components is observed in orientation number of 1-4 in Φ_2 = 0° section. Another low intensity of 1.27 of Cu {112} <111> texture is rotated to orientation number 6' in Φ_2 = 45° section. Other texture components are also observed from the orientation number 5-8. The S{123}<634> component with less intensity of 1.1 is rotated to an orientation number of 12 in Φ_2 = 65° section. Other texture components with slightly higher intensity are also observed in orientation numbers 9-11 and 13.

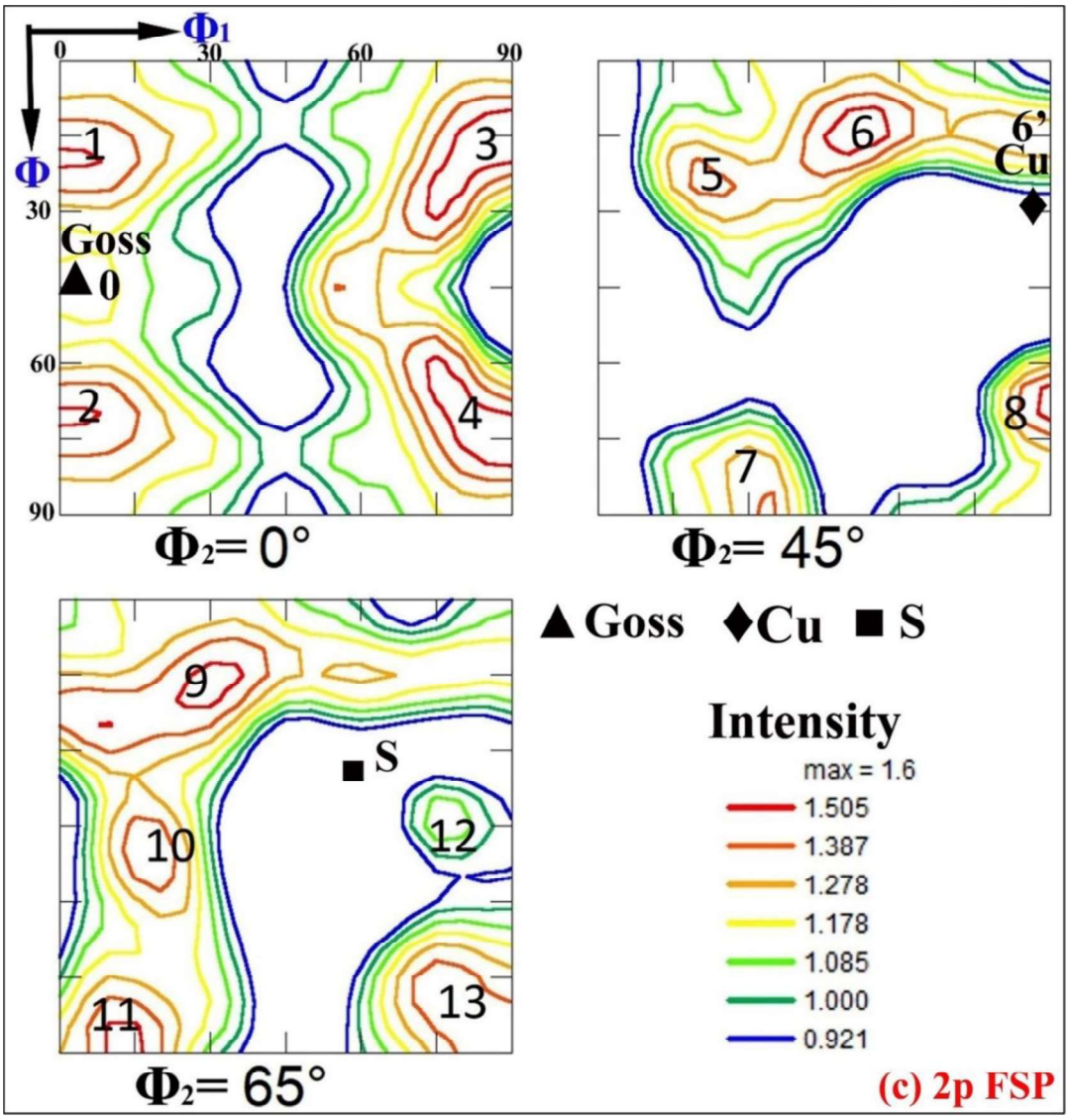

Figs. 5.3a-d Continued.....

The details of each texture component, their orientation, and the respective intensity values are given in Table 5.4.

Table 5.4 Texture components, orientation, and relative intensity after 2 pass FSP

Orientation No.	Texture components (h k l) [u v w]	Euler angles of orientation (Φ_1, Φ, Φ_2)	Intensity (x Random)
01	(0 1 3) [36 -3 1]	3.2°, 18.6°, 0.0°	2.1
02	(0 14 5) [1 0 0]	2.0°, 43.6°, 0.0°	2.4
03	(0 3 11) [1 $\overline{11}$ 3]	5.6°, 14.3°, 45.0°	2.5
04	(0 3 1) [2 $\bar{5}$ 15]	3.2°, 83.7°, 45.0°	2.3
05	(2 2 7) [6 $\overline{13}$ 2]	82.9°, 2.0°, 45.0°	1.5
06	(1 1 6) [$\bar{1}$ $\overline{11}$ 2]	88.8°, 76.5°, 45.0°	2.2
07	(10 10 1) [10 $\overline{11}$ 10]	1.6°, 87.2°, 45.0°	2.1
08	(5 5 3) [$\bar{3}$ $\bar{3}$ 10]	30.9°, 82.1°, 65.0°	1.5
09	(218) [$\bar{1}$ $\overline{22}$ 3]	70.2°, 1.6°, 65.0°	1.5
10	(212) [1 $\bar{4}$ 1]	70.2°, 1.6°, 65.0°	1.5
11	(14 6 1) [7 $\overline{17}$ 4]	70.2°, 1.6°, 65.0°	1.5
12	(425) [$\bar{7}$ $\bar{6}$ 8]	77.3°, 42.0°, 65.0°	1.1
13	(15 7 3) [$\bar{1}$ $\bar{3}$ 12]	78.9°, 79.3°, 65.0°	1.5

Fig. 5.3d displays ODF, Φ_2 = 0°, 45°, 65° sections of NZ, after 3pass FSP. The texture intensity slightly increases to 2.1 times random as compared to the 2 pass FSP of 1.6 times random. The Goss {011} <100> texture of 2.0 times random is observed in orientation 1, corresponding to Φ_2 = 0° section. Other texture components with a reduced intensity of 1.21 are seen in orientation numbers 2 & 3. The Cu {112} <111> texture is rotated to orientation number 4 in Φ_2 = 45° section. Added to this, rotated Goss texture {110} <110> of 1.9 times random is also observed in orientation number 5. The S {123} <634> texture component of 1.9 times random is rotated to orientation number 6 in Φ_2 = 65° section. Another texture component is also seen in the orientation number of 7.

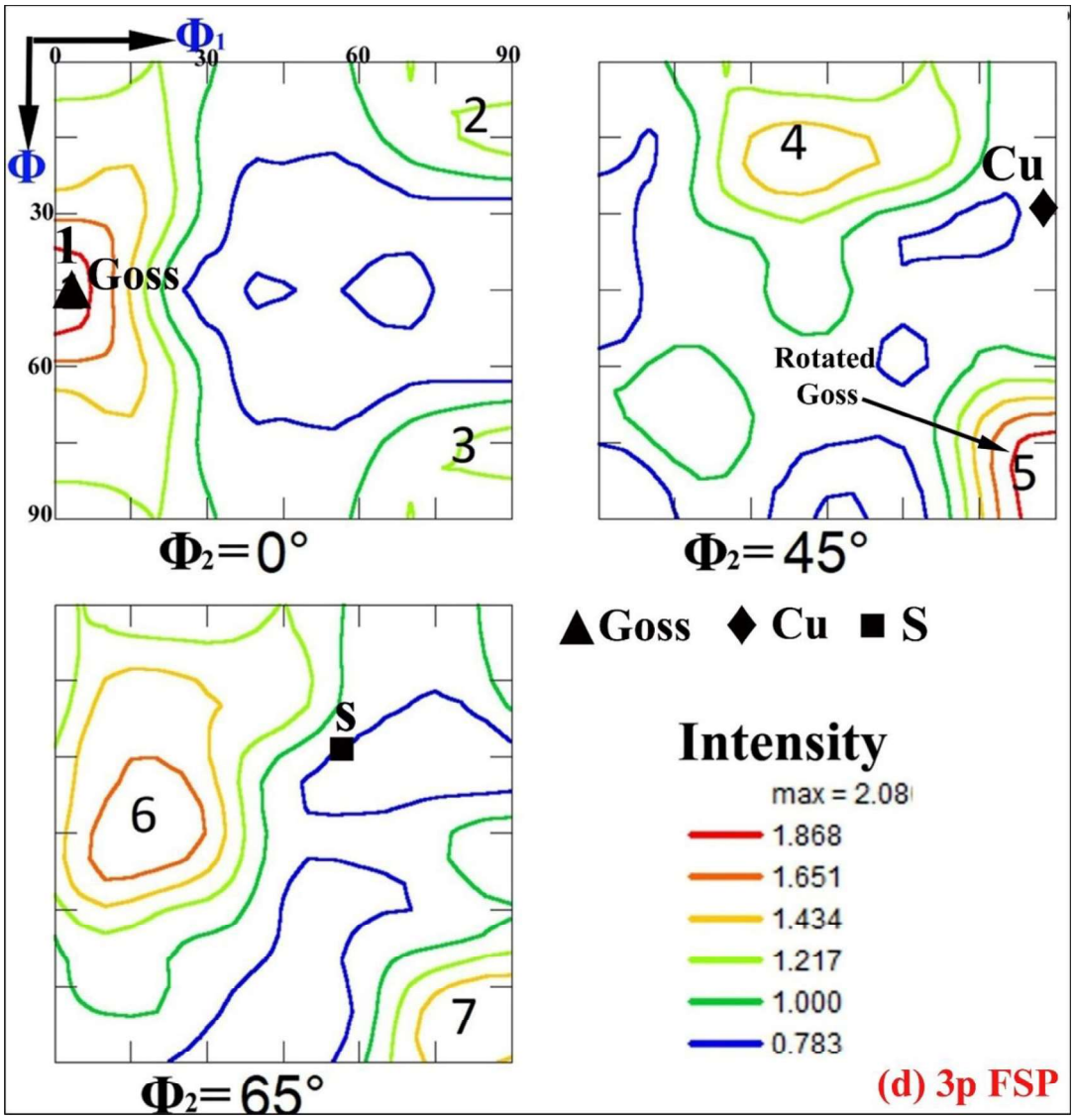

Figs. 5.3a-d Continued.....

The details of each texture component, their orientation, and respective intensity values are given in Table 5.5.

Table 5.5 Texture components, orientation, and relative intensity after 3pass FSP

Orientation No.	Texture components (h k l) [u v w]	Euler angles of orientation (Φ_1, Φ, Φ_2)	Intensity (x Random)
01	(0 1 1) [1 0 0]	0°, 45.0°, 0.0°	2.0
02	(0 12 13) [1 $\overline{13}$ 12]	86.4°, 11.1°, 0.0°	1.3
03	(1 1 6) [32 $\overline{38}$ 1]	85.6°, 77.3°, 0.0°	1.3
04	(18 17 3) [14 $\overline{15}$ 1]	38.5°, 17.8°, 45.0°	1.6
05	(0 0 1) [$\overline{7}$ $\overline{9}$ 0]	86.8°, 78.9°, 45.0°	2.0
06	(1 1 23) [$\overline{11}$ $\overline{12}$ 1]	17.0°, 41.6°, 65.0°	1.8
07	(16 7 18) [3 $\overline{12}$ 2]	82.1°, 80.5°, 65.0°	1.6

Grain size of AR alloy, and after FSP (1pass, 2pass, and 3pass) are given in Figs. 5.4a, c, e, g. This is measured to be 54±3 μm in the AR state. On the other hand, 4.0±0.5 μm, after 1 pass FSP, followed by 3.5 ±0.6 μm, after 2 passes, and 2.6±0.4 μm, after 3pass FSP. Corresponding grain boundary fractions are given in Figs. 5.4b, d, f, h. The low and high-angle grain boundary fractions in AR alloy are 85% (LAGBF) and 15% (HAGBF) respectively. After 1pass FSP, the LAGBFs are 51% and the HAGBFs are 49%. After 2pass FSP, the LAGBFs are 53%, whereas, HAGBFs are 47%. The LAGBFs after 3 pass FSP are 70%. On the other hand, HAGBFs are 30%.

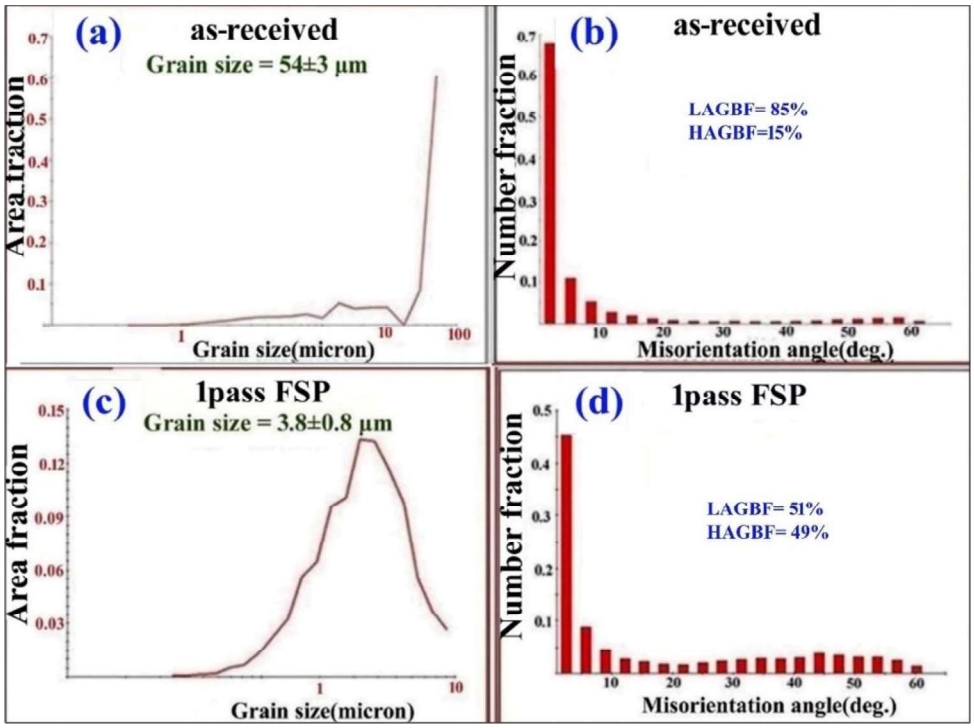

Figs. 5.4 a-h. Grain size, and mis-orientation angle plot of multi-pass FSP: (a,c,e) grain size versus area fraction maps, and (b,d,f) misorientation angle vs. number fraction maps**.**

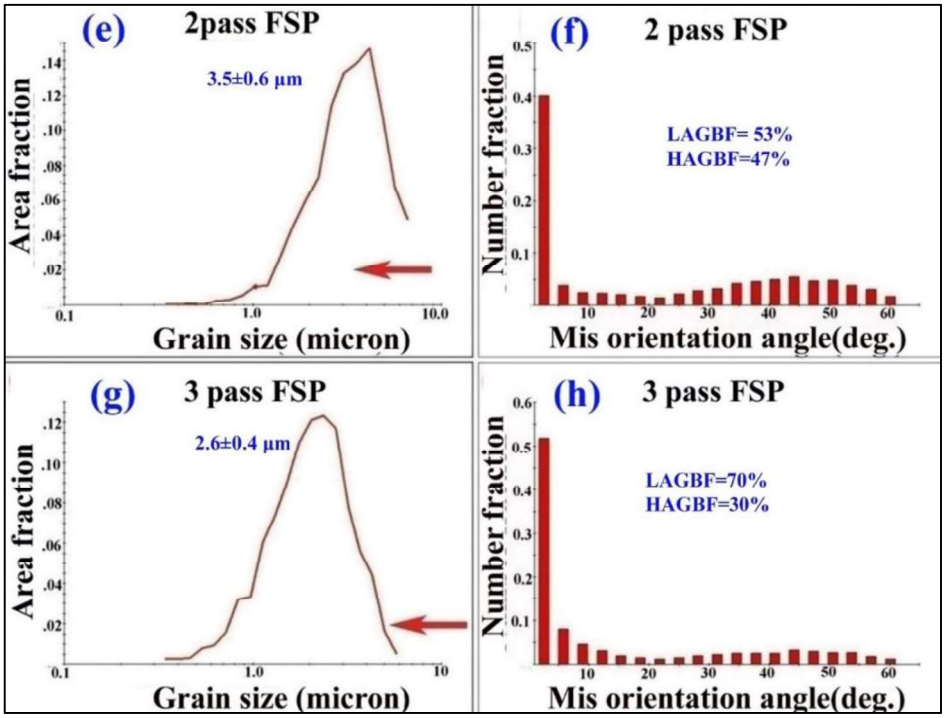

Figs. 5.4a-h Continued……

Fig. 5.5a-d shows the IPF map of AR alloy and after FSP (1pass, 2pass, and 3pass). The 111 crystal plane of α-Al, shows preferred orientation along RD in the AR alloy (Fig. 5.5a). The 001 crystal plane is the preferred orientation after 1pass FSP (Fig. 5.5b). The 110 of α-Al depicts the preferred orientation along RD after 2pass FSP (Fig. 5.5c). The 111 crystal plane of α-Al displays the preferred orientation along RD after 3pass FSP (Fig. 5.5d). Respective IPF maps are given in the inset of the figures.

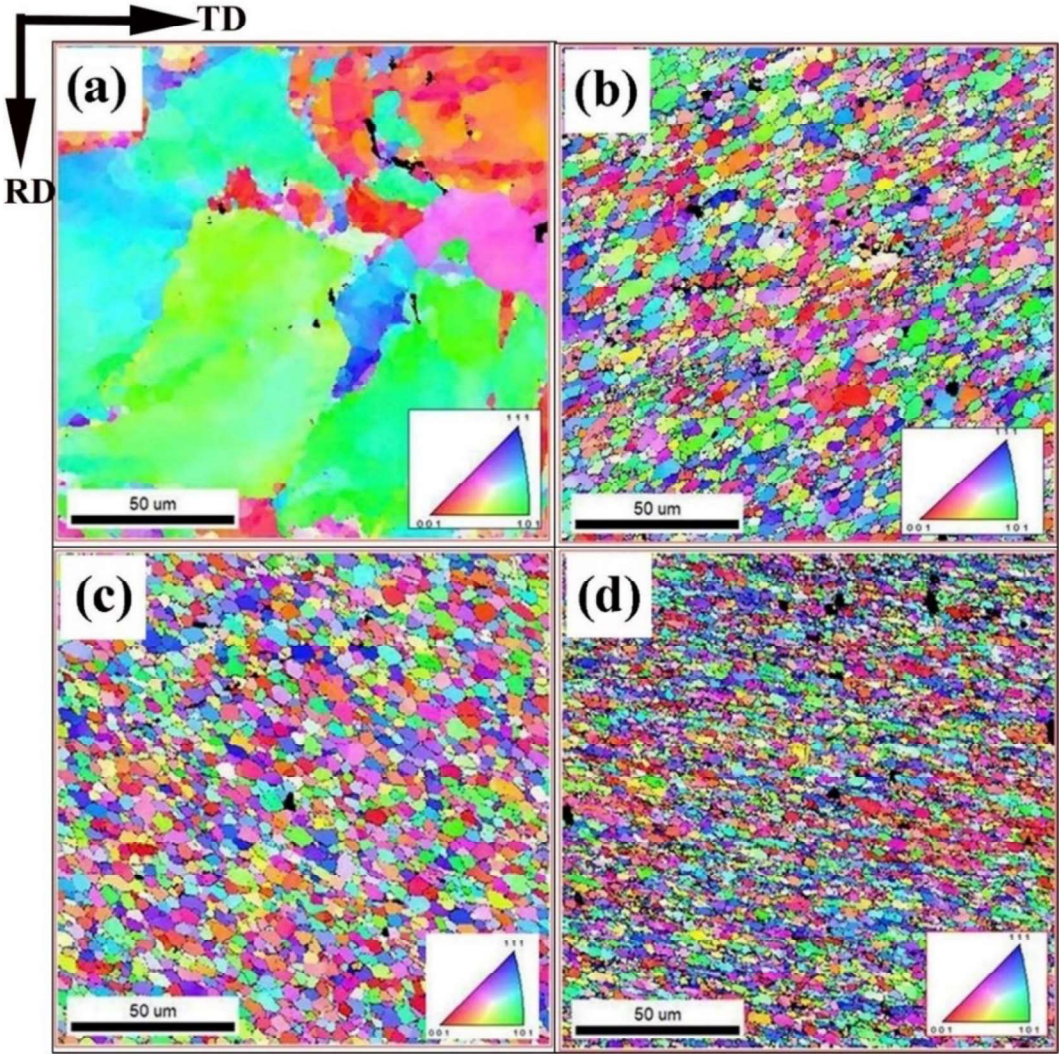

Figs. 5.5a-d. Micro-texture characteristics/color-coded grain maps: (a,b,c,d) inverse pole figure map, and (e,f,g,h) KAM map of AR alloy and after 1pass FSP, 2pass FSP and 3 pass FSP.

Fig. 5.6a-d shows the pole figure (PF) of AR alloy and after FSP (1pass, 2pass, and 3pass) respectively. The maximum intensity in the AR alloy is 5.9 times random (Fig. 5.6a) which decreases to nearly 2.0 times random after 1pass FSP (Fig. 5.6b). On the other hand, 1.4 times random (Fig. 5.6c) and 1.6 times random (Fig. 5.6d) after 2pass, and 3pass FSP respectively. This indicates that FSP randomizes the texture component. The 111 pole figure shows more intensity in the AR state. The 200 PF shows more intensity after 1pass FSP. On the other hand, the 220 and 111 PF display high intensity after 2 passes and 3 passes of FSP, which is consistent with the XRD analyses, and the IPF maps.

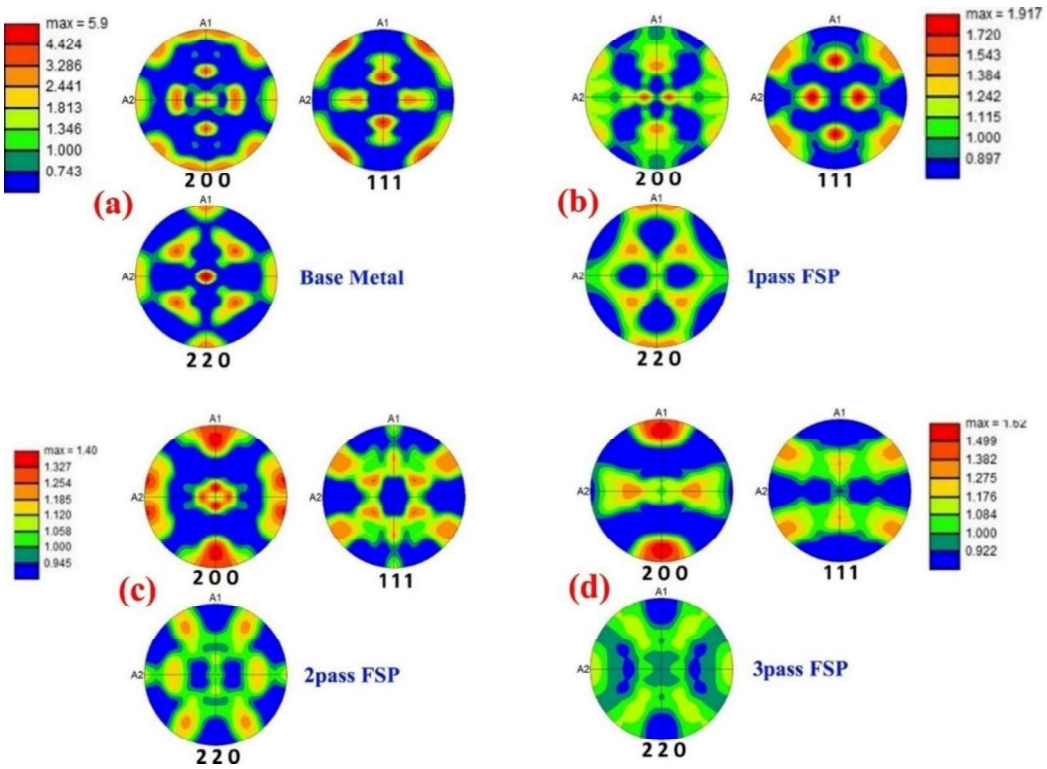

Figs. 5.6a-d 111, 200, and 220 pole figures of (a) base metals, (b) 1pass FSP, (c) 2pass FSP, and(d) 3pass FSP. A1 displays the rolling direction, and A2 shows the transverse direction.

Figs. 5.7a-d shows the Kernel average misorientation (KAM) maps of AR alloy and after FSP, (1pass, 2pass, and 3pass) respectively. The average KAM of AR alloy is 0.52 (Fig. 5.7a). After 1pass FSP, the average KAM increases to 0.56 (Fig. 5.7b). The average KAM value after 2pass FSP is 0.45 (Fig. 5.7c). On the other hand, the KAM value after 3 passes of FSP is 0.65 (Fig. 5.7d).

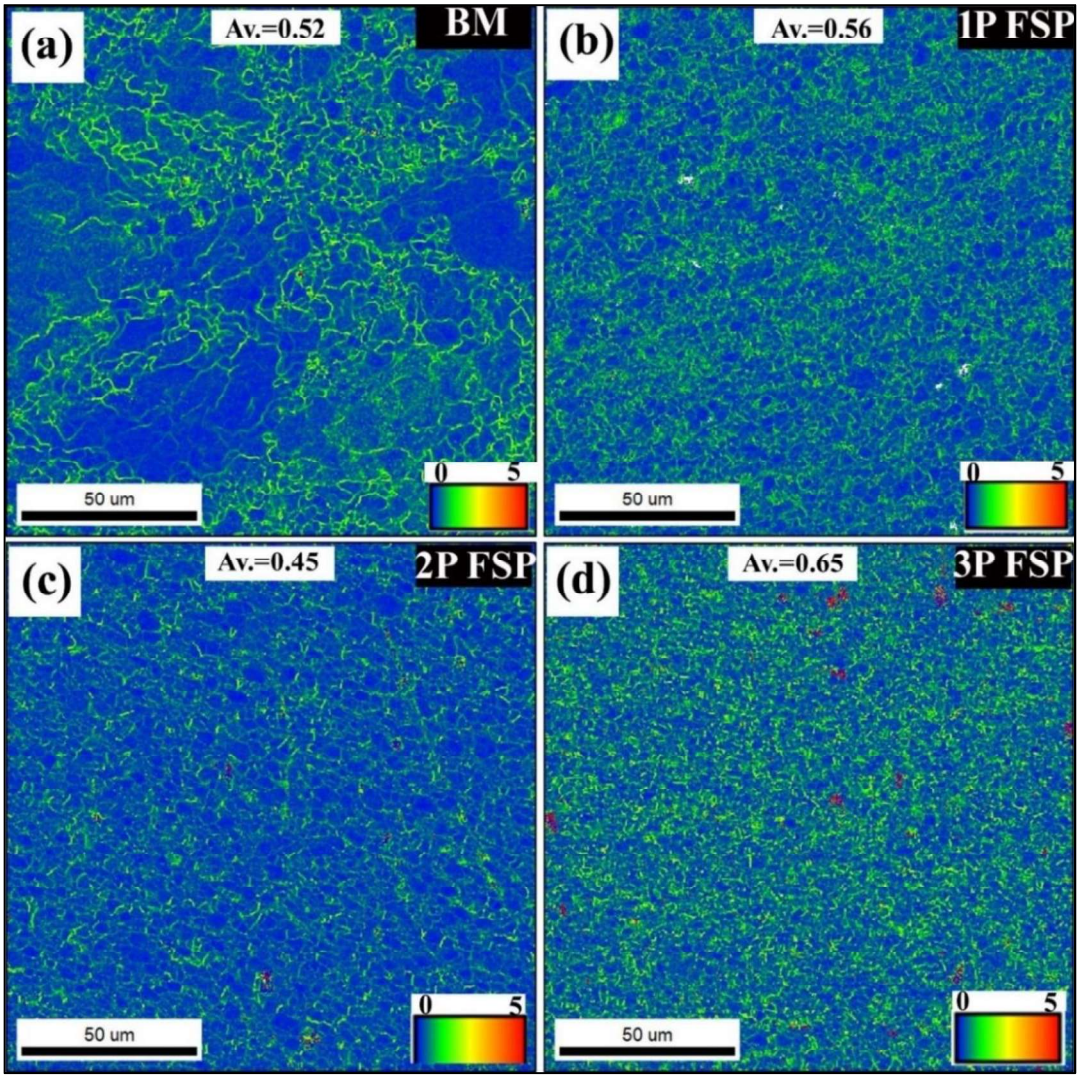

Figs. 5.7a-d Kernel average misorientation (KAM) maps of (a) AR alloy (BM), (b) 1 pass FSP, (c) 2 pass FSP, and (d) 3 pass FSP.

Figs. 5.8a-d shows co-incident site lattice (CSL) boundary maps of AR alloy and after FSP (1pass, 2pass, and 3pass) respectively. The co-incidence site lattice (CSL) fractions of Σ3, Σ5, and Σ9 in the AR alloy are 0.75, 0.19, and 0.35 respectively (Fig. 5.8a). After 1pass FSP the CSL boundary (Σ3, Σ5, and Σ9) fractions are 1.25, 0.65, and 0.55 alternatively (Fig. 5.8b). After 2pass FSP, the corresponding CSL boundary (Σ3, Σ5, and Σ9) fractions are 1.35, 0.95 and 0.85 (Fig. 5.8c). On the other hand, respective CSL boundary fractions after 3pass FSP are 1.0, 0.65, and 0.55 (Fig. 5.8d).

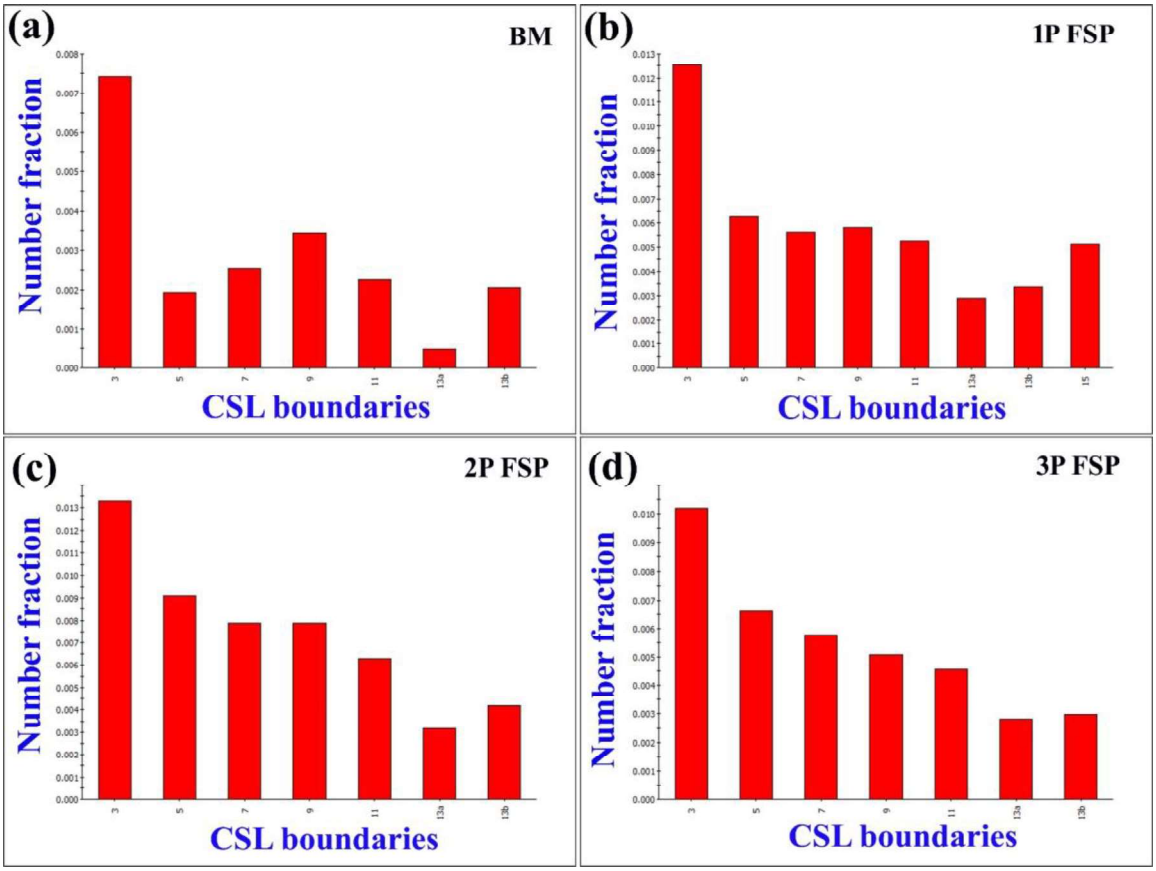

Figs. 5.8a-d. Coincident site lattice (CSL) boundary fractions for (a) AR alloy, (b) 1pass FSP, (c) 2pass FSP, and (d) 3pass FSP.

5.2.4 TEM Analysis

5.2.4.1 TEM analysis after 1 pass FSP

Fig. 5.9a displays a bright-field TEM (BF-TEM) micrograph from one of the regions of AR alloy. The rod, and plate-like morphologies of η' and η, are seen in this. Corresponding, SAEDPs~ are shown in Fig. 5.9b. The sharp crystalline DPs~200 of α-Al, with 4-fold symmetry, are noticed. Another weak satellite-like DPs~of the η' and η (Laves phases of C14 type) with 4-fold symmetry are also observed. Fig. 5.9c displays a bright-field TEM (BF-TEM) micrograph from another region. The presence of the η' and η are major observations. Corresponding SAEDPs are given in Fig. 5.9d. The sharp crystalline diffraction spots (DPs~), 220 of α-Al, are seen respective to1.43Å (d-spacing). Other weak crystalline spots of η' and η (Laves phases of C14 type & hP12 structures) are also observed respectively to d-spacing values of 2.11 Å, and 1.91 Å.

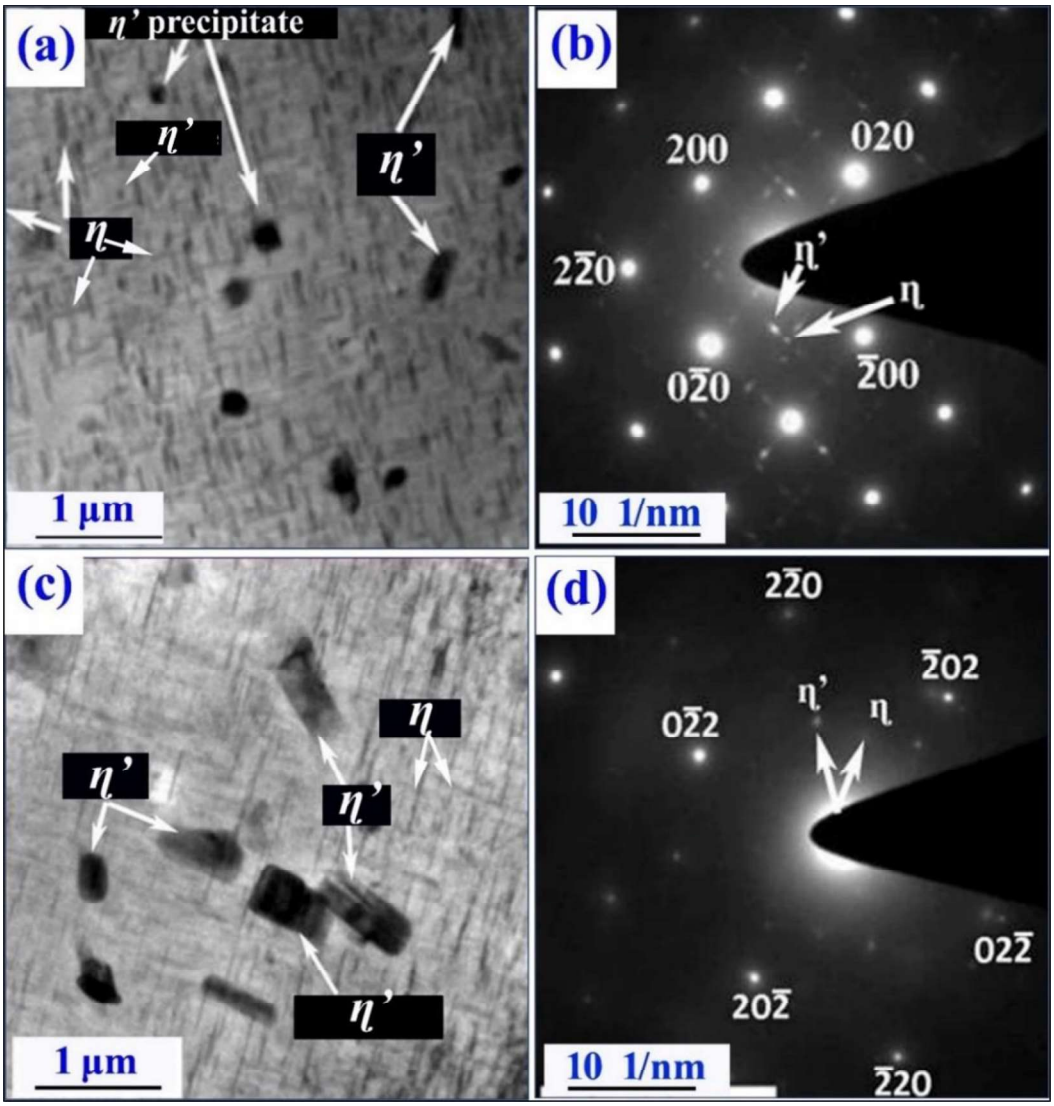

Fig. 5.9a-d bright field TEM micrograph, and corresponding SAEDPs of AR alloy: (a,b) along 001 of α-Al, (c,d) along 110 of α-Al.

Nearly~ 10% compressive deformation is given to AR alloy. This generates a sufficient amount of dislocation inside the α-Al matrix. Therefore, systematic tilting (using α and β) is done to obtain the weak beam condition to study the dislocation structures. Fig. 5.9e displays a bright-field TEM micrograph of AR alloy in 3-beam conditions. The presence of dense / forest dislocation is observed. Respective SAEDPs~ are given in Fig. 5.9f. The existence of the sharp and weak crystalline spots, 111 of the α-Al, are noticed in the 3-beam condition.

Intense spots display the strong beam, whereas weak spots depict the weak beam. Fig. 5.9g displays a weak-beam dark-field (WBDF) TEM micrograph from "2g". The presence of the dense/ forest dislocation is mainly observed. Fig. 5.9h shows WBDF-TEM micrograph from "3g". The dense dislocation walls (DDWs~) are a major observation.

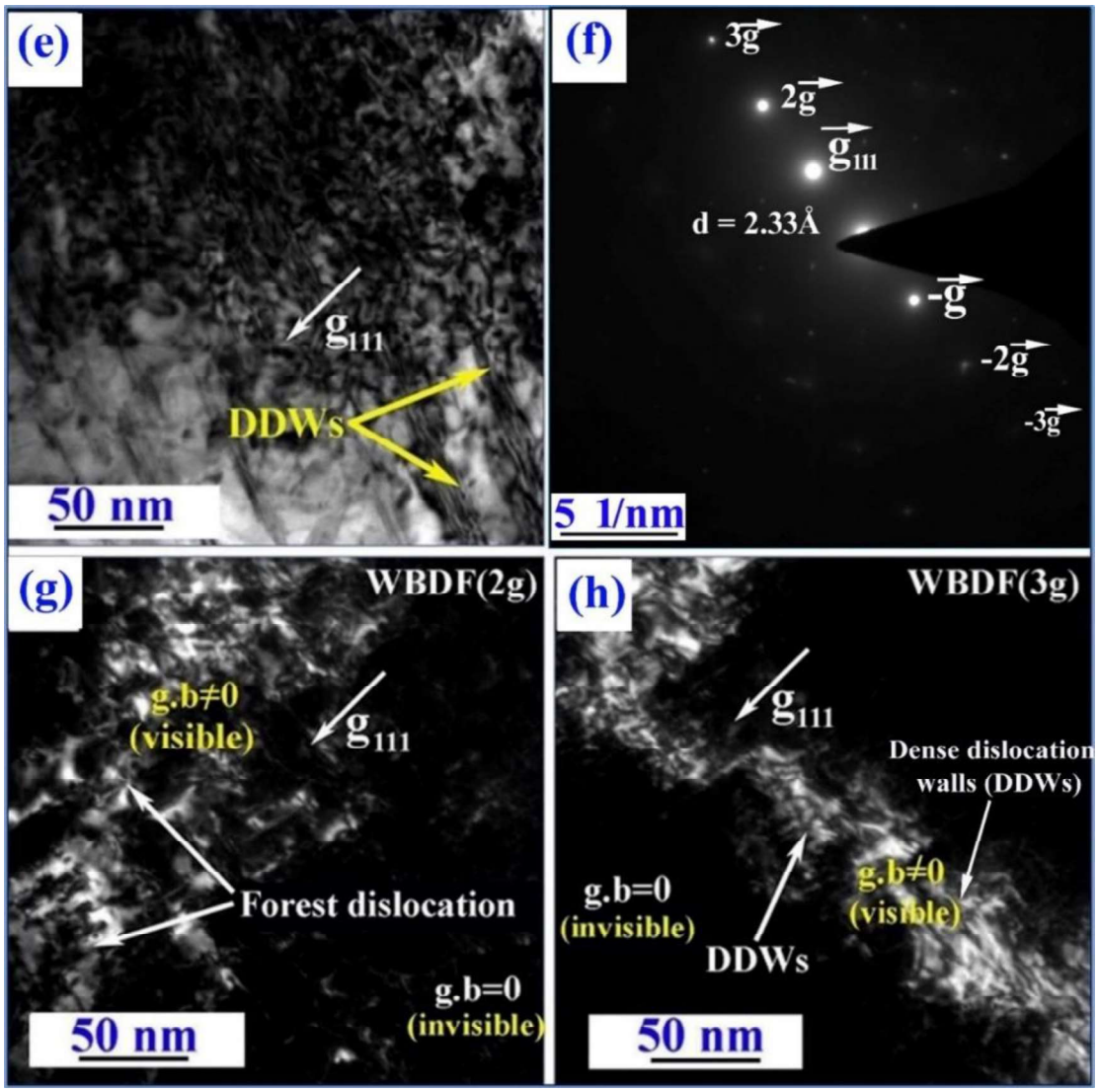

Fig. 5.10e-h. Dislocation behavior: (e) bright-field TEM micrograph, (f) corresponding DPs~, (g, h) WBDF-TEM micrograph from the g and 2g, respectively.

Dislocation structures are noticed at the top of the nugget zone. Therefore, systematic dislocation characterization is done with the help of the WBDF-TEM Imaging technique. The suitable tilting of α and β brings weak-beam requirements. After getting the 2g and 3g beams, the tilting is stopped, and dark field TEM imaging is done from the higher-order weak-diffracted spots alternatively. Fig. 5.11a displays the BF TEM image, from the top of the NZ. Dislocation peening and a parallel array of dislocation are mainly observed. Respective SAEDPs~ are given in Fig. 5.11b. The sharp DPs (200) of α-Al (d~2.02Å, PDF# 77-1177) in 2 beam conditions are observed. Intense spot (g) displays the strong beam. On the other hand, the weak spot (2g) depicts the weak beam. Fig. 5.11c depicts WBDF-TEM micrograph from diffracted spot “g". The presence of the wavy dislocation array and dislocation peening are the major observations. Added to this, the recovered dislocation structures are also seen in some portions. Fig. 5.11d shows the WBDF-TEM micrograph from the diffracted spot "2g". The evolution of the dense wavy dislocation array and the recovered microstructures are observed.

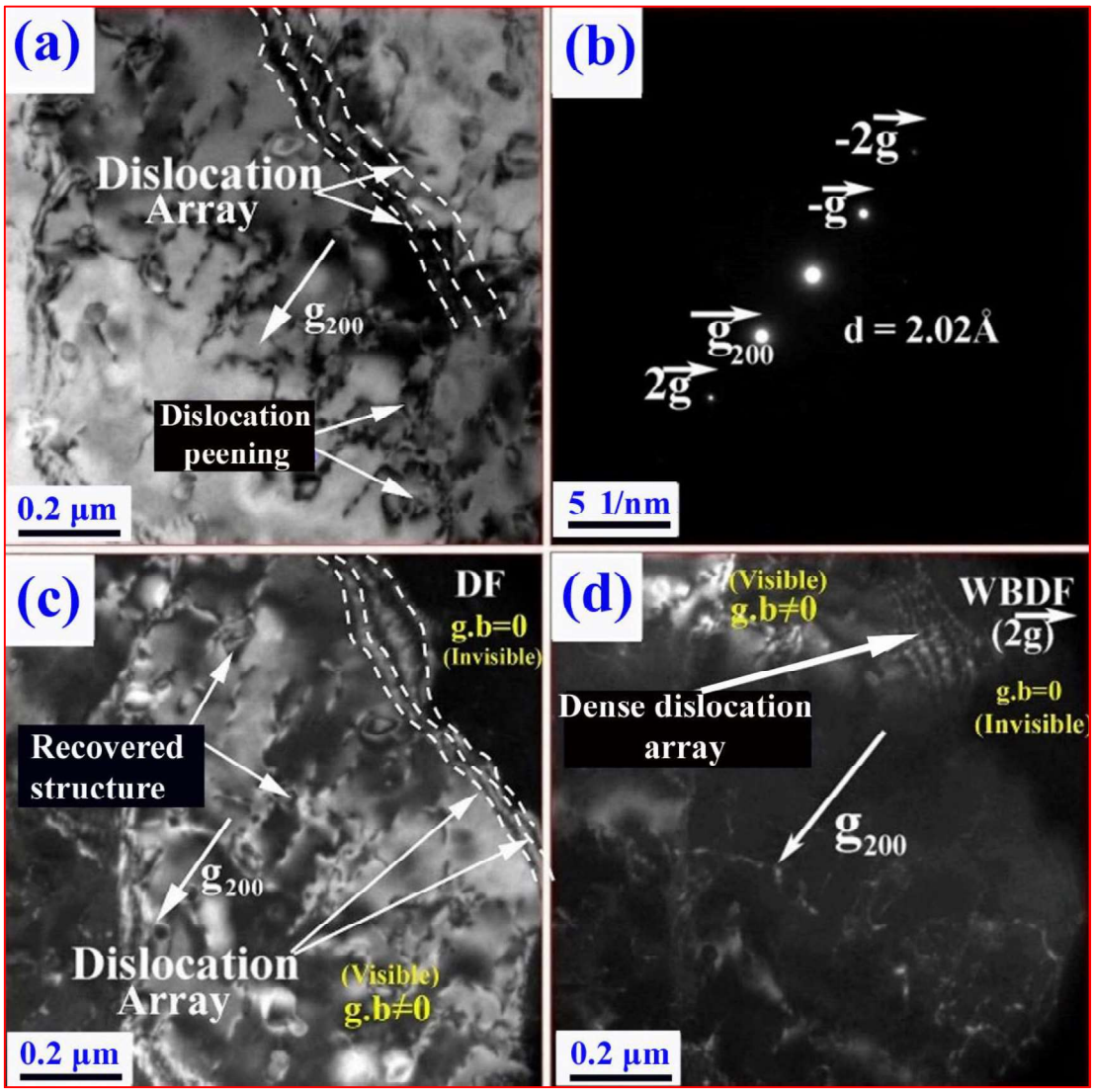

Figs. 5.11a-d bright-field TEM micrograph of top of nugget-zone (a), respective SAEDPs (b), dark field TEM micrograph from g (c), and DF TEM micrograph from 2g (d).

Fig. 5.12a shows a bright-field TEM micrograph from a middle portion of the NZ. Evolution of the dislocation network (hexagonal and tetragonal) and dislocation peening are observed. Respective SAEDPs~ are given in Fig. 5.12b. The sharp and weak DPs (200) of α-Al can be seen in the 3-beam condition. Fig. 5.12c displays WBDF-TEM micrograph from diffracted spot "2g". A parallel array of dislocation, and dislocation networks (hexagonal and tetragonal) are notable features. Added to this, dislocation peening structures are also

observed. Fig. 5.12d portrays the WBDF-TEM micrograph respective to the diffracted weak spot "3g". A parallel array of dislocation with low density and dislocation network are the major observations.

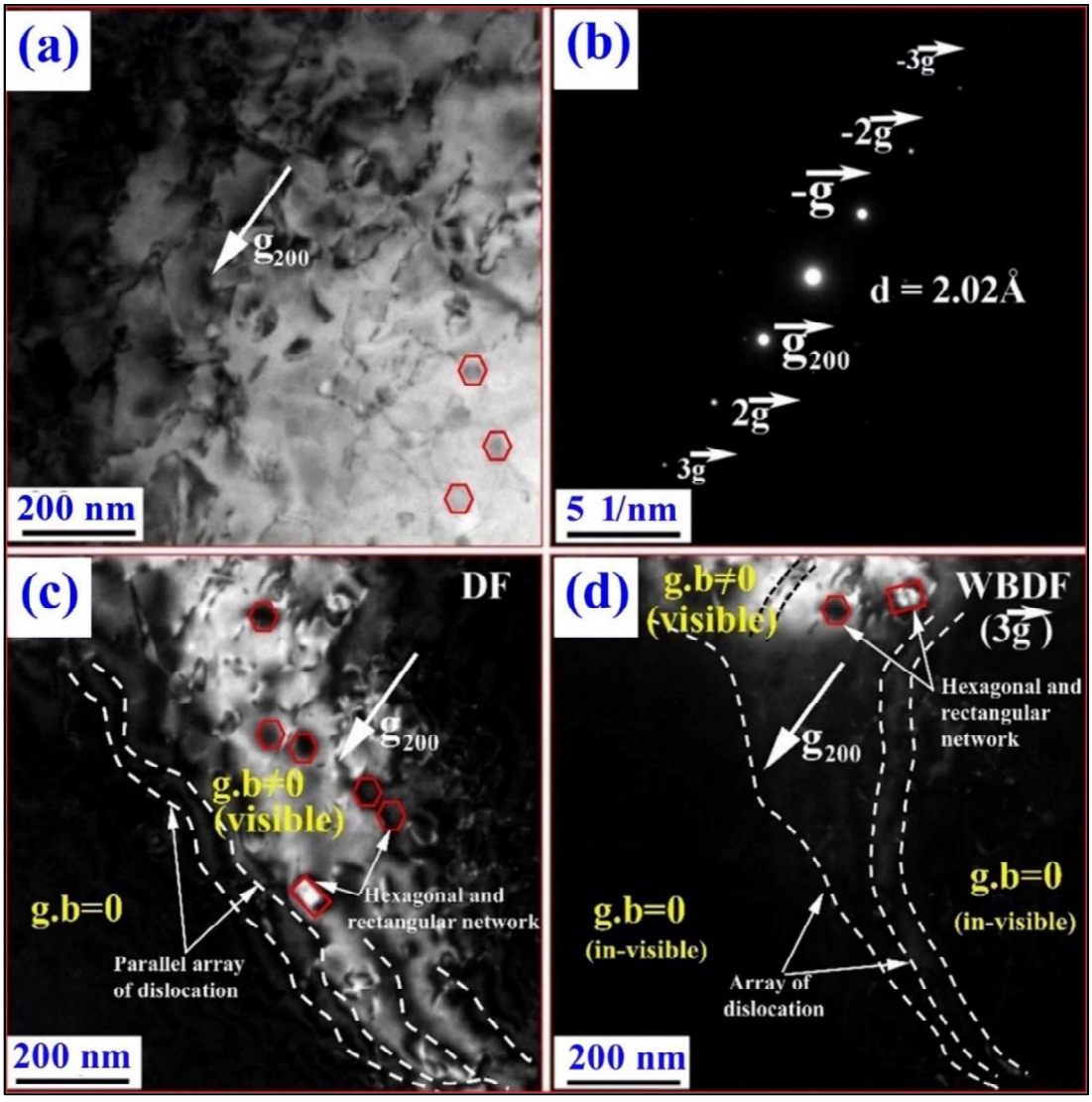

Figs. 5.12a-d. Dislocation behavior from a middle portion of the NZ: (a) bright-field TEM micrograph, (b) respective SAEDPs in 3-beam condition, (c) WBDF-TEM micrograph from "2g", and (d) WBDF-TEM micrograph from "3g".

Fig. 5.13a shows a bright-field TEM micrograph, from a bottom portion of the NZ. The presence of the sub-grain structure with dense dislocation is observed close to the sub-grain boundary. The inside subgrain boundary shows dense dislocation structures. On the other hand, a parallel array of dislocation is noticed close to the boundary. The outside sub-grain boundary is free from dislocation and contains the precipitates (*η' and η*). Corresponding SAEDPs~ are given in Fig. 5.13b. The sharp and weak crystalline DPs (200) of α-Al are mainly observed. Fig. 5.13c displays the BF-TEM micrograph from another region. The sub-grain boundary with dense dislocation structures is observed. Some of the subgrain boundaries are free of dislocation and contain the precipitates. Respective SAEDPs~ are given in Fig. 5.13d. The sharp and weak spots (200) of α-Al, in the 3-beam condition are the major observations.

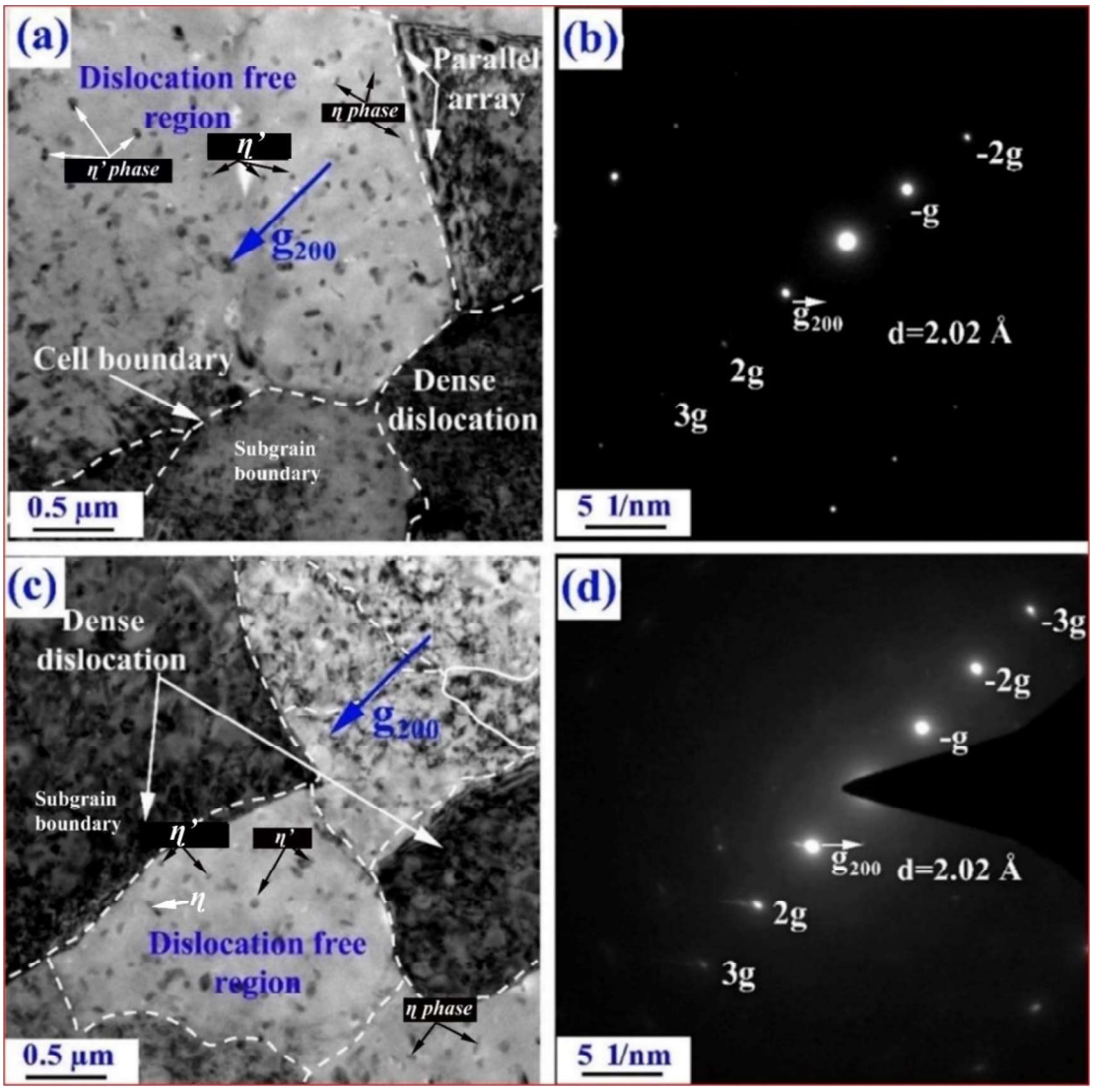

Figs. 5.13a-d Precipitates morphology and dislocation behavior at the interface after FSP: (a, c) bright-field TEM micrographs, and (b,d) corresponding SAEDPs~.

5.2.4.2 TEM analysis after multipass FSP

Fig. 5.14a shows a bright field TEM micrograph, from one of the regions of AR alloy. The presence of differently oriented η' (rod), and η (plate) precipitates are observed. Respective SAEDPs~ are given in Fig. 1b. The sharp spots of α-Al, and weak spots of η' and η precipitates with 4-fold symmetry are the major observations. The dark-field TEM

micrograph taken from the weak spot marked by the white arrow depicts the presence of plate type η precipitates differently oriented towards the 110 and $1\bar{1}0$ of the α-Al.

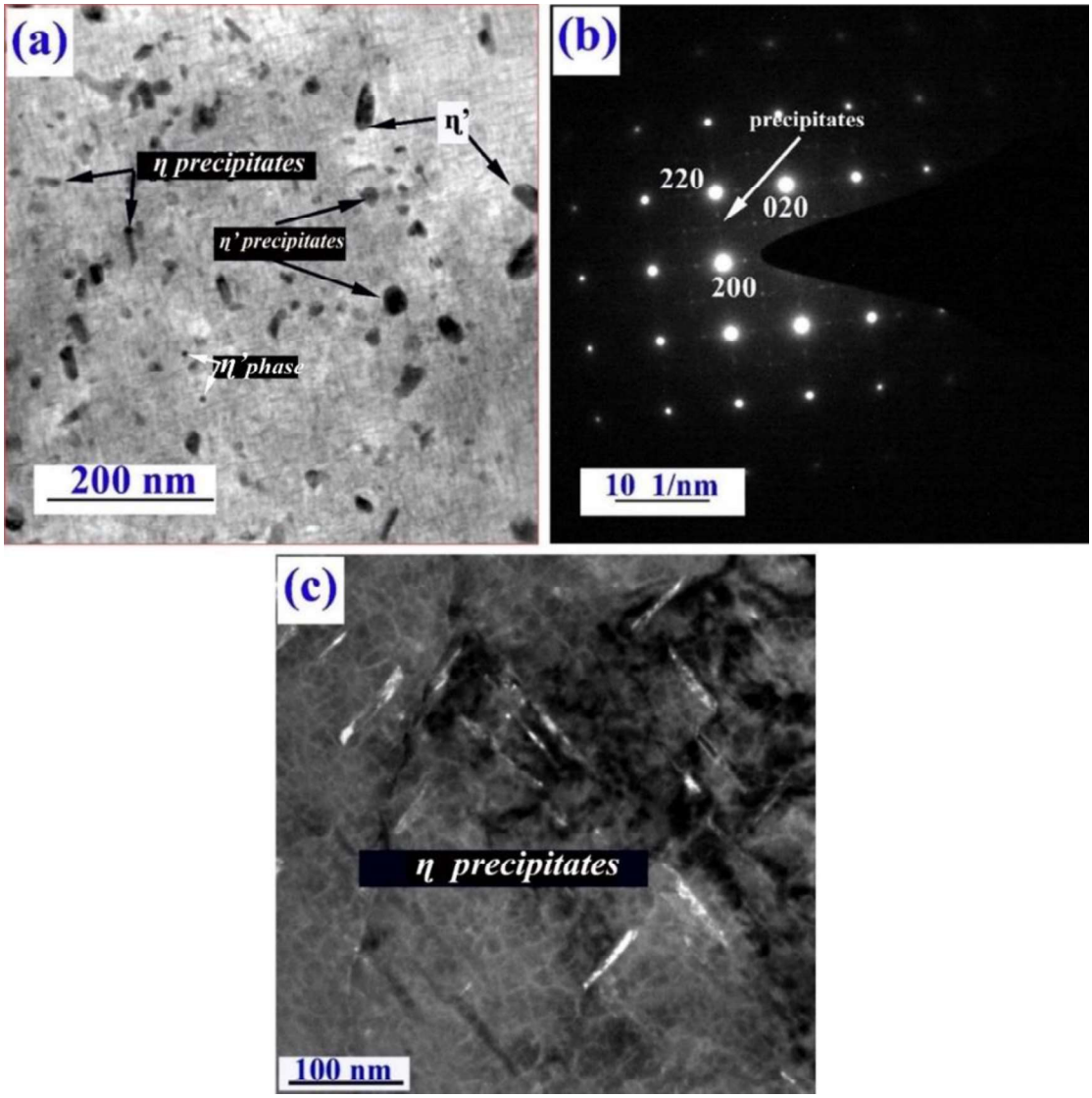

Fig. 5.14a-c TEM micrograph of as-received specimen: (a) bright-field TEM images, (b) corresponding SAEDPs~, (c) dark field TEM image.

Fig. 5.14.1a displays a bright-field TEM micrograph from two separate regions of the top of the NZ. The evolution of the recovered microstructure and strain-field region is observed. Corresponding SAEDPs~ are given in Fig. 5.14.1b. The sharp DPs (200 and 220) of α-Al

are only observed corresponding to the d-spacing value of 2.02 Å and 1.43 Å respectively. Fig. 5.11c shows a bright-field TEM micrograph from another region. The presence of the dislocation network and strain-field region is another major observation. Respective SAEDPs~ are given in Fig. 5.11d. The sharp crystalline DPs (200, and 220) of α-Al, are observed. On the other hand, DPs of the η' and η are absent.

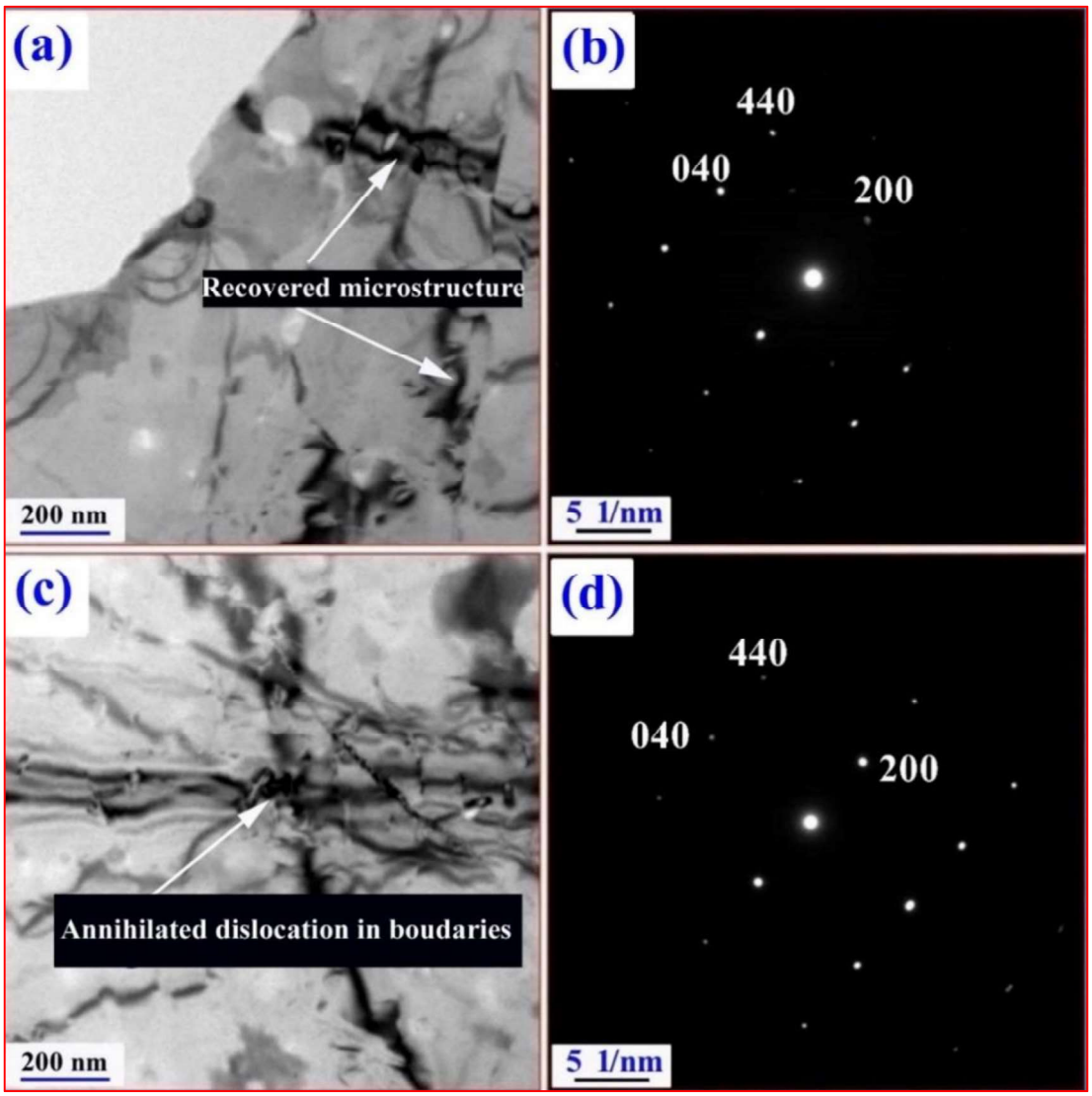

Figs. 5.14.1 (a, c) bright-field TEM micrographs of a top portion of the NZ, and (b, d) respective DPs.

Figs. 5.15a displays a bright field TEM micrograph after 2pass FSP. The presence of the tangled dislocation as well as η precipitates are mainly observed. On the other hand, the GP zone and η' are absent in the α-Al matrix. Fig. 5.15b shows the corresponding SAEPDs. The sharp spots of α-Al with 6-fold symmetry and the weak spots of η precipitates are seen. The dark field TEM micrograph taken from a weak spot marked by the white arrow displays the presence of the η phase in Fig. 5.15c. On the other hand, η' are absent.

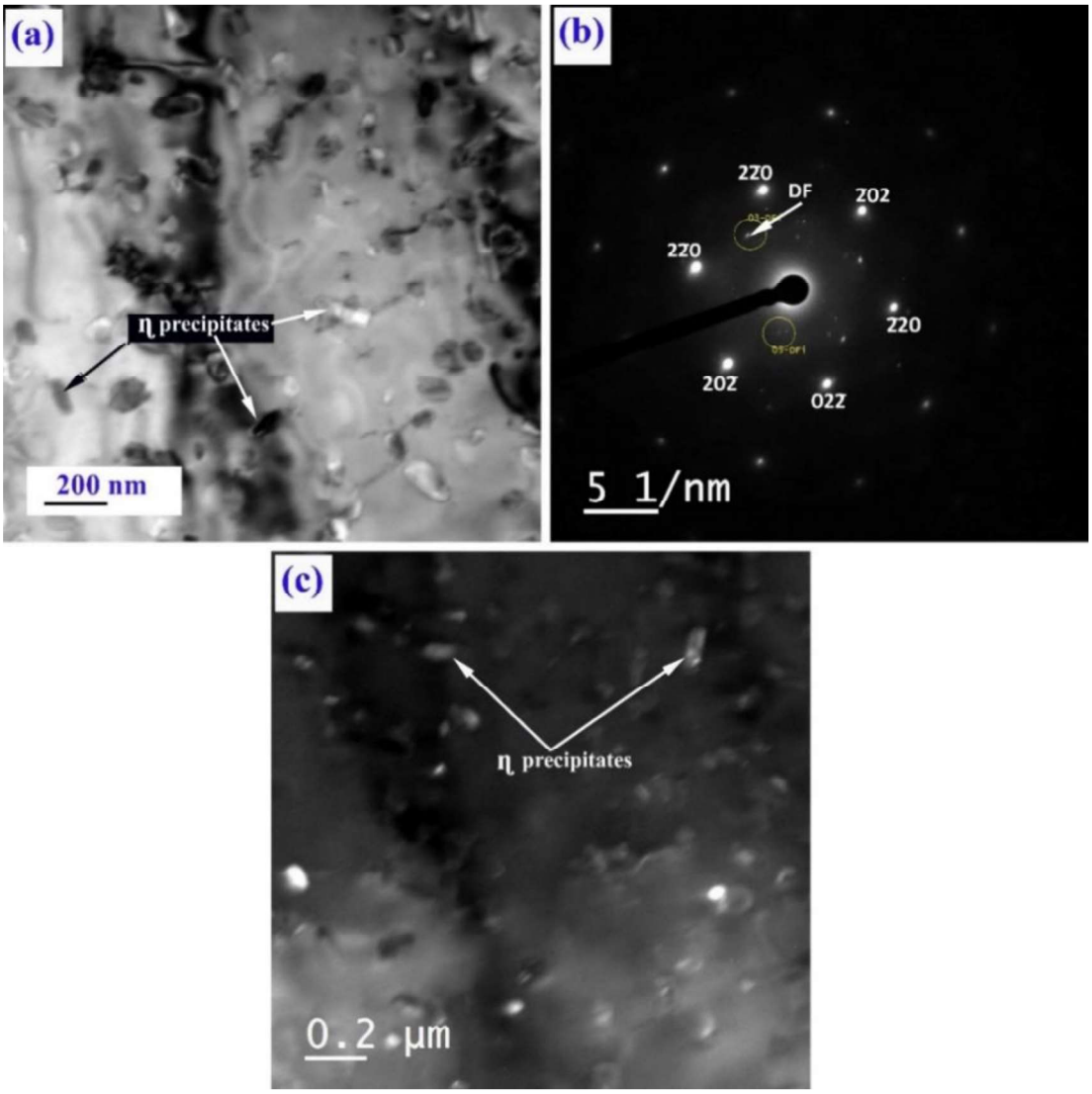

Figs. 5.15a-c TEM micrograph, after 2pass FSP, along 111 of α-Al: (a) bright-field TEM image, (b) corresponding SAEDPs, (c) dark field TEM micrograph.

Figs. 5.16a shows a bright field TEM micrograph after 3pass FSP. The presence of the dislocation and η'(rod), and η (plate) are the mainly observed. Fig. 7b depicts corresponding SAEPDs. The sharp spots of α-Al with 6-fold symmetry and the weak spots of η' and η are seen. Dark field TEM micrograph taken from the weak spot marked by the white arrow displays the presence of η' precipitates in Fig.7c.

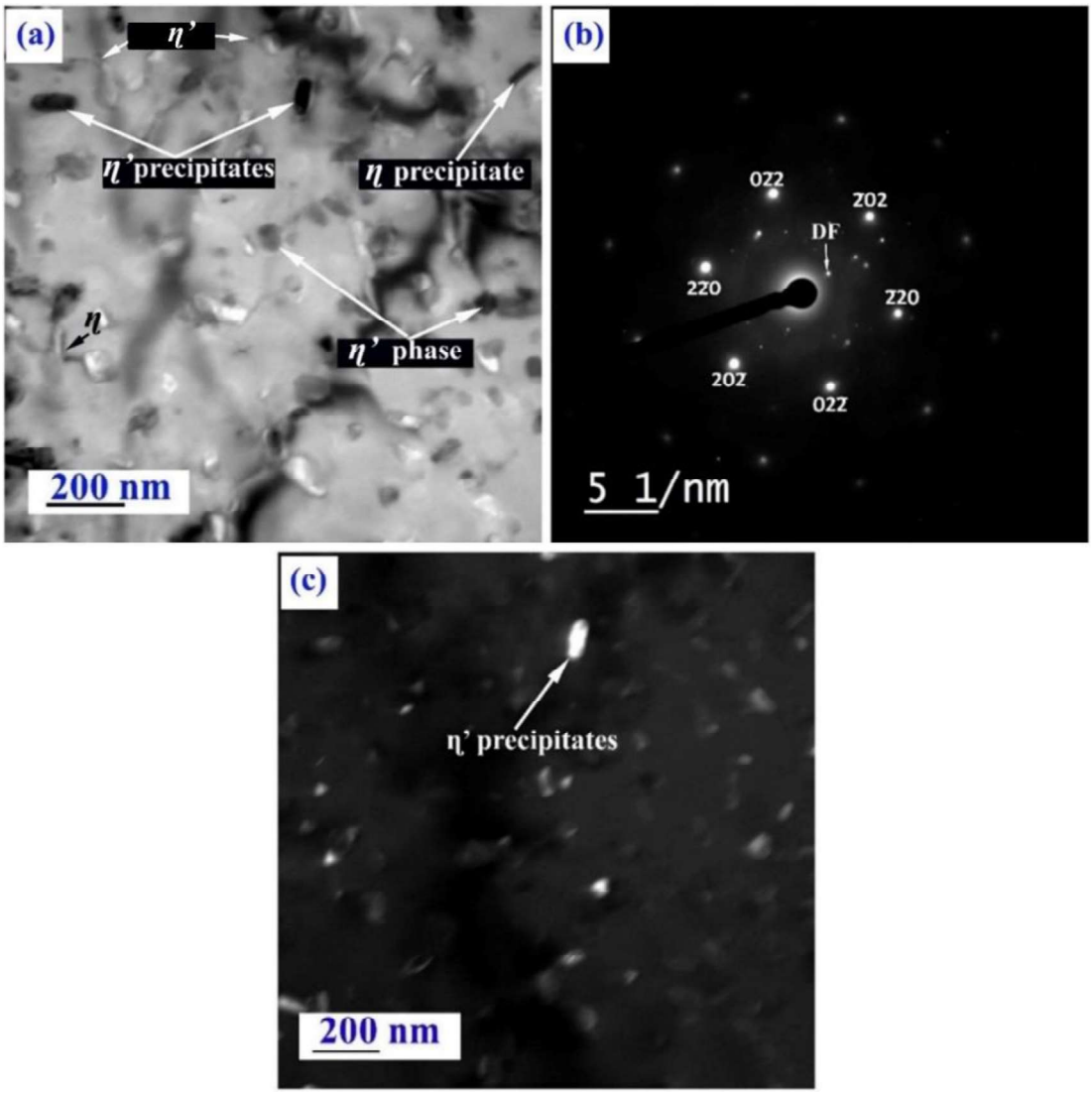

Figs. 5.16a-c TEM micrograph, after 3pass FSP, along 111 zone-axis of α-Al: (a) bright-field TEM image, (b) corresponding SAEDPs, (c) dark field TEM image.

Fig. 5.17a-h shows the bright and dark field STEM micrograph, for AR alloy, and after FSP (1pass, 2pass, 3pass respectively). The presence of the η' and η are observed in AR alloy (Fig. 5.17a,b), in addition to the Al_2CuMg intermetallic. After 1pass FSP the η at 2θ=20°is not observed (Fig.5.17c,d). On the other hand, the presence of the η' and η are observed in addition to the Al_2Cu, Al_2CuMg, and $Al_{23}CuFe_4$. After 2 passes of FSP, η' and ηprecipitates are seen in addition to the Al_2Cu and Al_2CuMg but their number density is less and size is reduced also confirming the dissolution of phases (Fig. 5.17e,f). After 3pass FSP, re-precipitation of the ηis observed in addition to the η' but their contrast is different from the AR condition (Fig. 5.17g-h) showing changes in the chemistry of the precipitates.

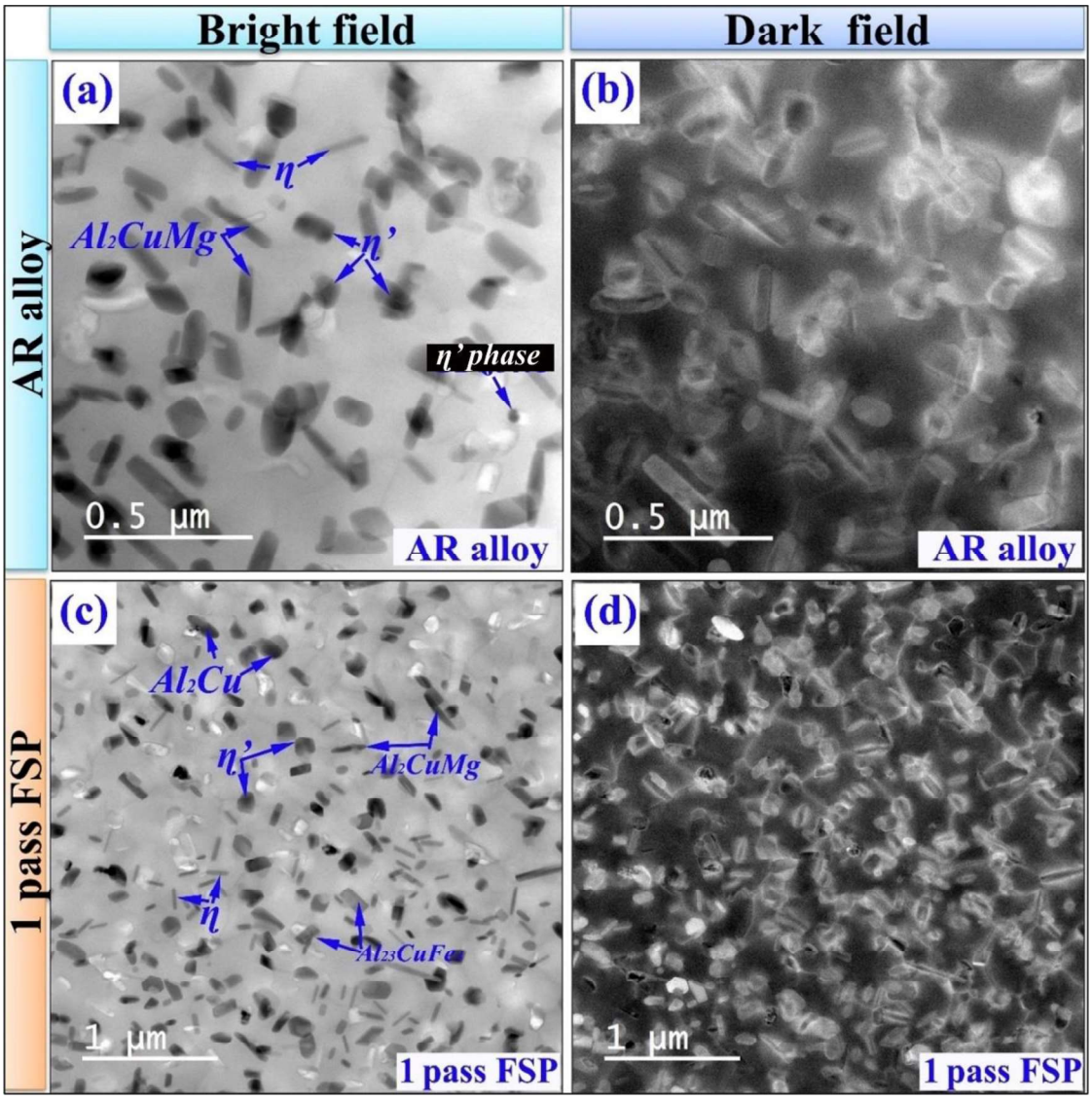

Fig. 5.17a-h Bright and dark field STEM micrograph of (a, b) AR alloy, (c,d) 1pass FSP, (e,f) 2pass FSP, (g,h) 3pass FSP.

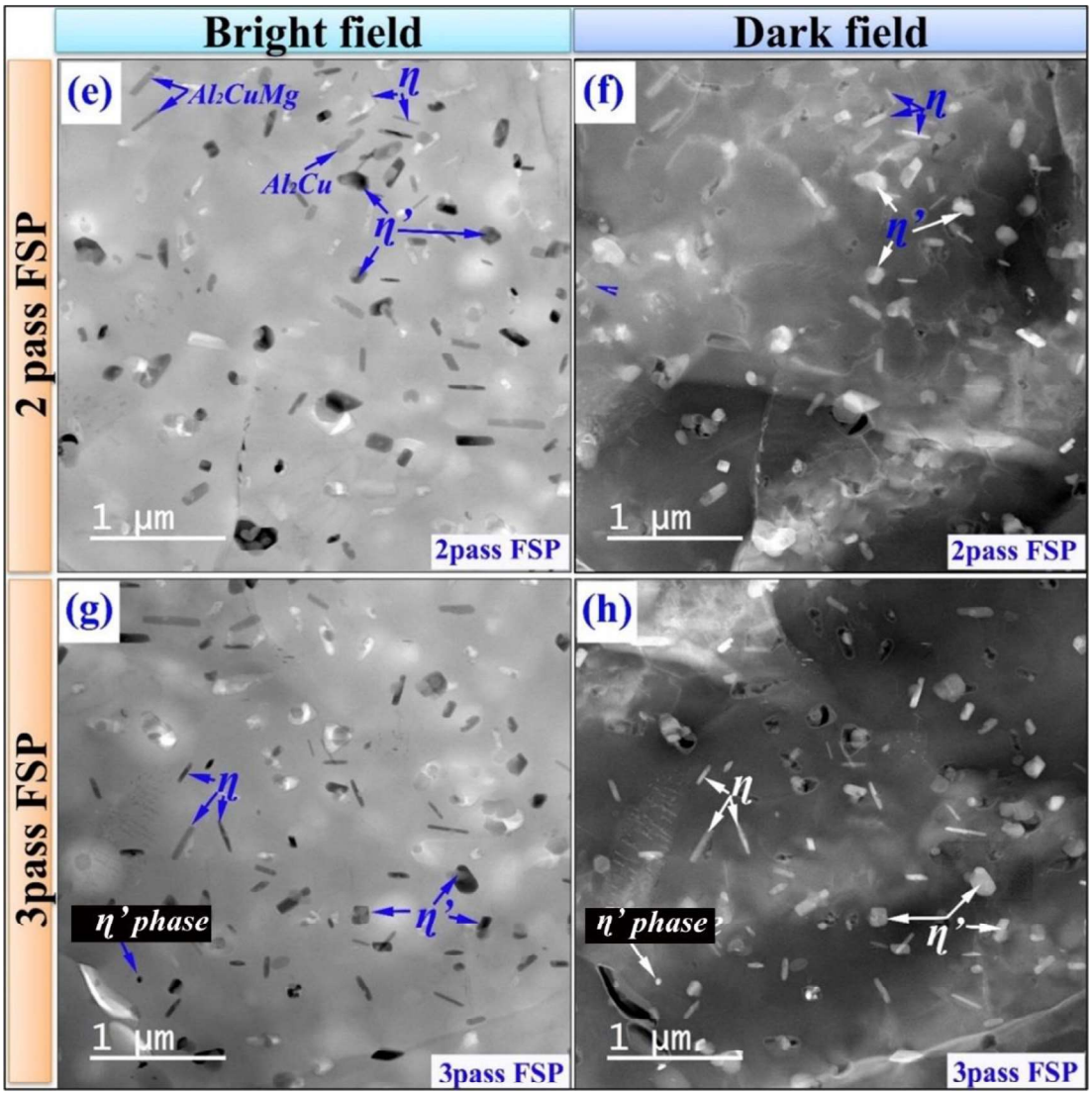

Fig. 5.17a-h Continued……

5.2.5 STEM EDS elemental mapping

Fig. 5. 18a shows a bright field TEM micrograph in the AR state. The presence of the spherical morphology of the rod type morphology of η', and plate morphology of η precipitates are mainly observed. The corresponding area spectrum mapping of precipitates is given in Fig. 5.18b, which is consistent with the chemistry of precipitates in the AR condition. The respective elemental mapping of precipitates is given in Fig. 5.19a-i. The

presence of precipitates rich in Mg, Zn, and Cu are mainly observed. On the other hand, precipitates also confirm the elemental presence of Cr, Si, Zr, and Mn but their magnitude is very low.

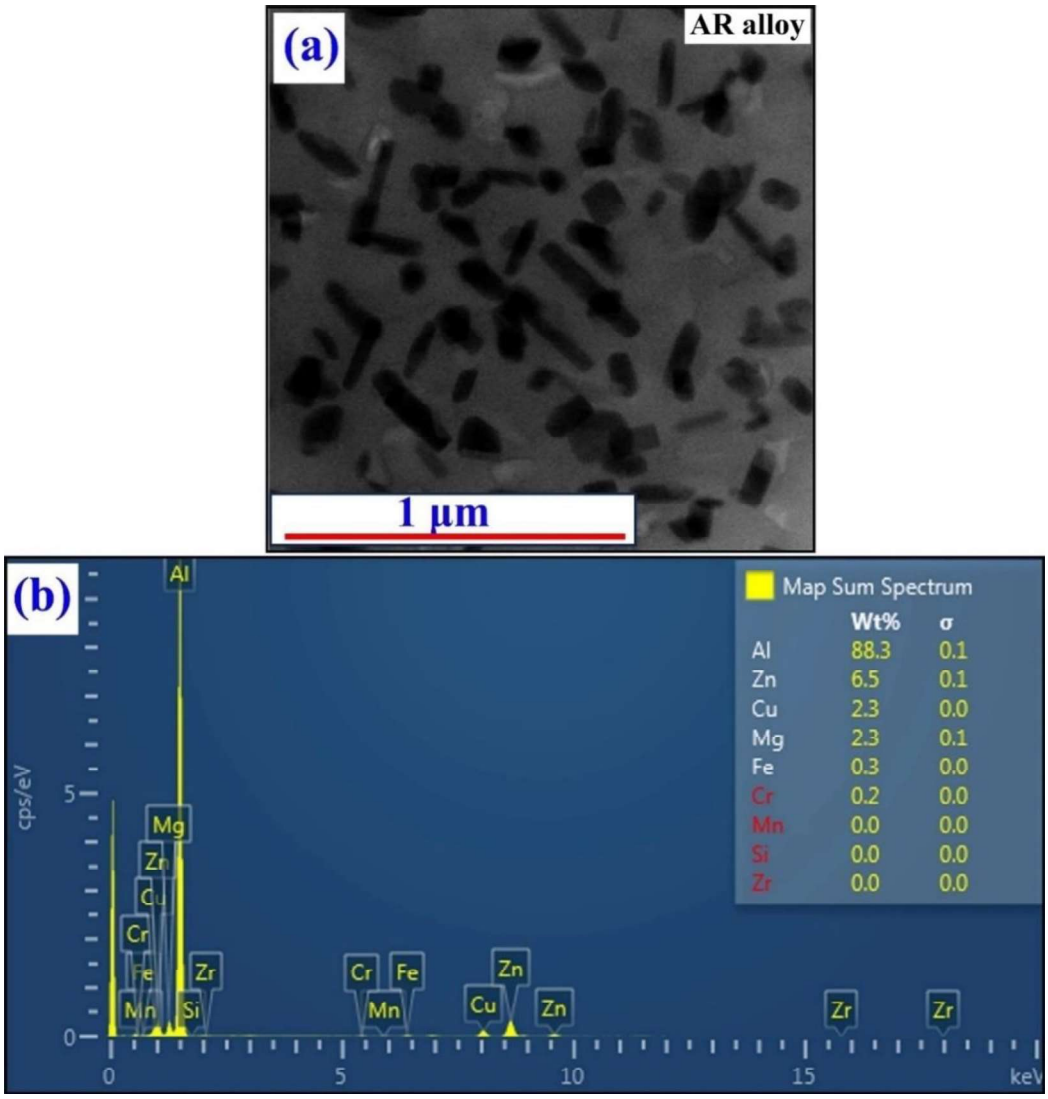

Fig. 5.18a-b Spectrum area mapping of precipitates in AR state: (a) bright-field STEM micrograph, (b) spectrum of elements in a selected area of precipitates.

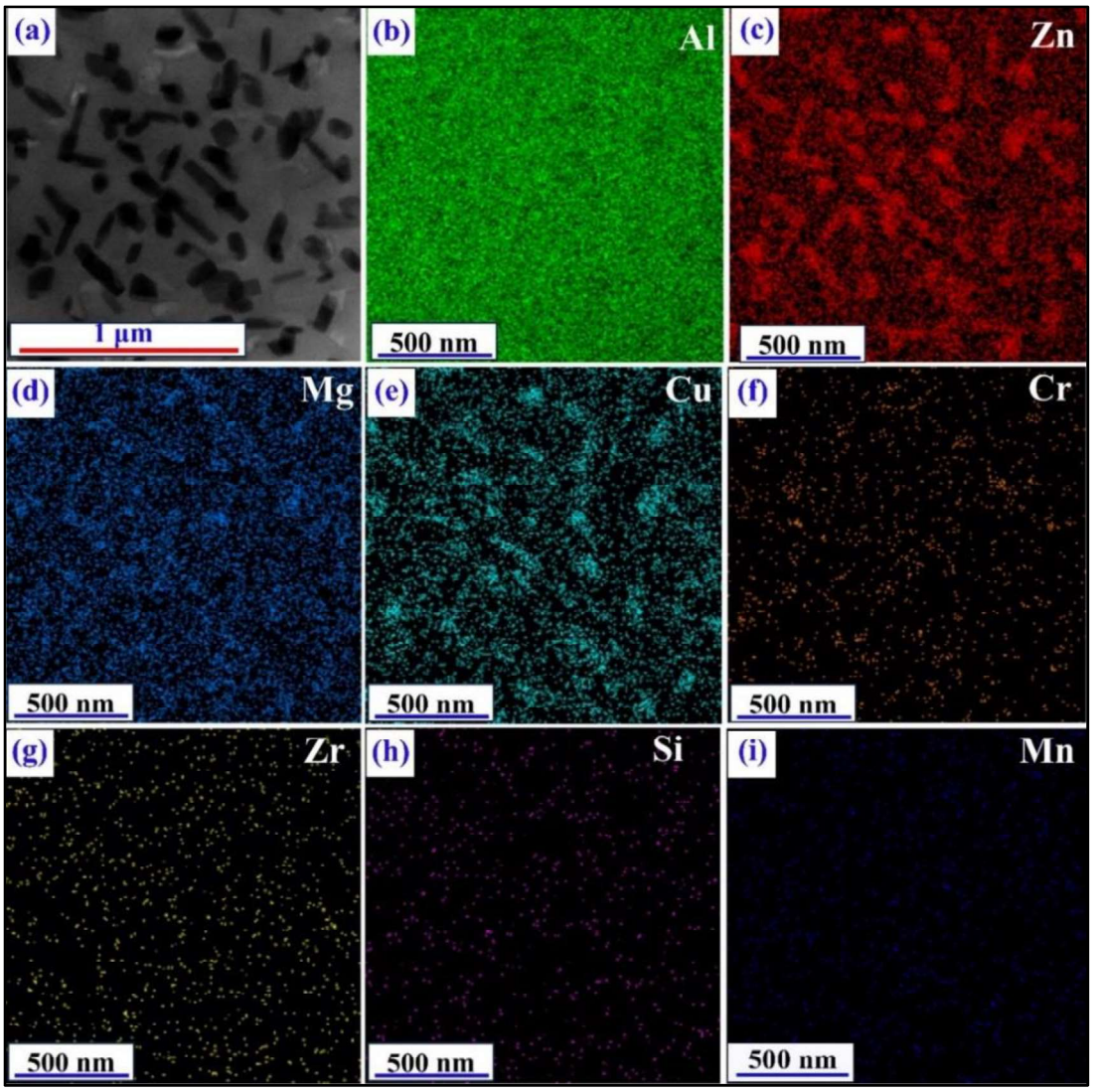

Fig. 5.19a-i STEM-EDS elemental mapping of precipitates in AR state: (a) bright-field STEM micrograph, (b) map of Al, (c) Zn, (d) Mg, (e) Cu, (f) Cr, (g) Zr, (h) Si, (i) Mn.

Fig. 5.20a shows a bright-field STEM micrograph in the AR state. The presence of η' (rod-morphology), and η (plate-morphology) are mainly observed. The corresponding area spectrum mapping of precipitates is given in Fig. 5.20b. Changes in the chemistry of precipitates are observed as compared to AR conditions. The analyzed chemistry confirms precipitates lean with Zn and Cu and indicates the dissolution of phases. The chemistry of precipitates after elemental mapping is given in Fig. 5.21a-i. The presence of precipitates

rich in Mg, Zn, and Cu are mainly observed but their contrast is less than the AR condition.

Precipitates also depict the elemental presence of Cr and Fe but their magnitude is very low.

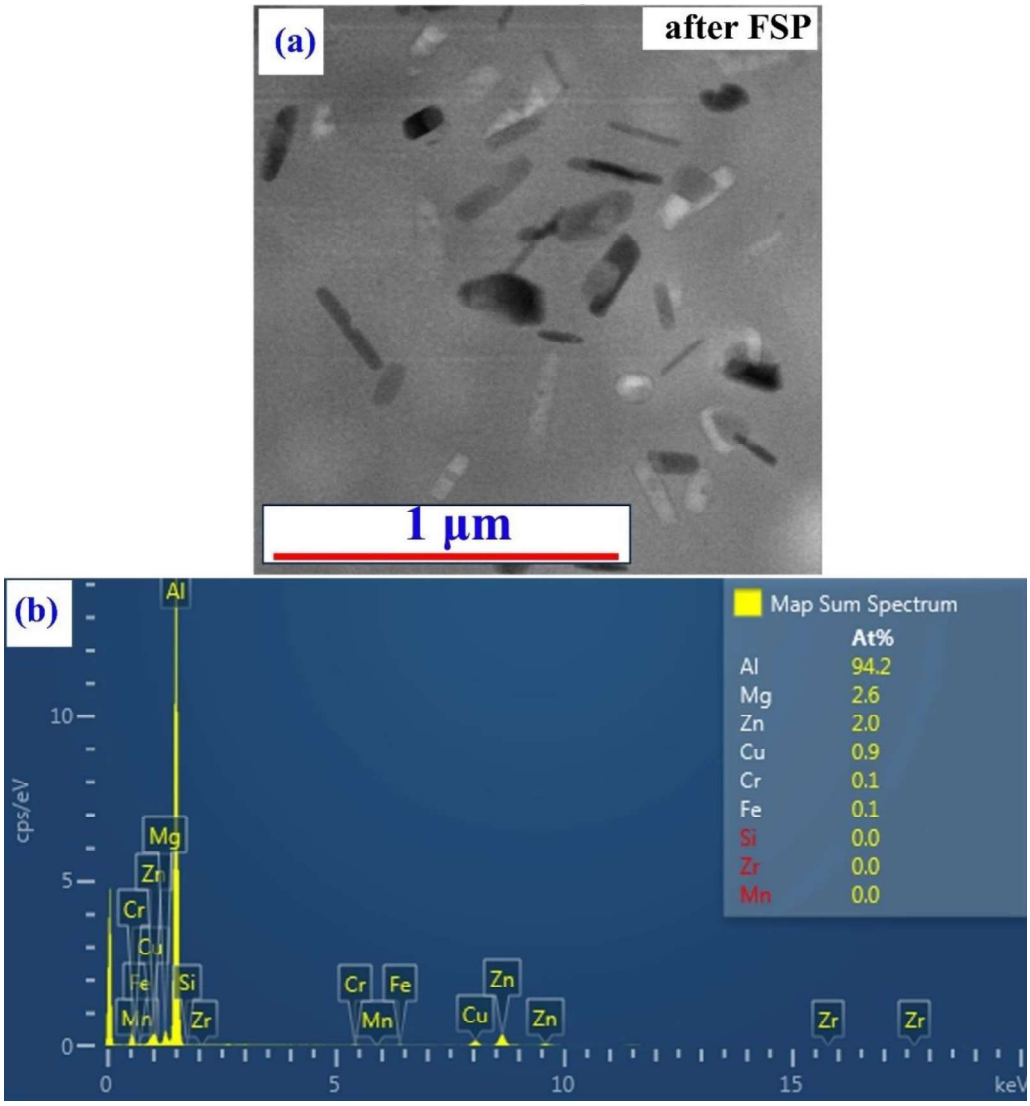

Fig. 5.20a-b Spectrum area mapping of precipitates after FSP: (a) bright-field STEM micrograph, (b) spectrum of elements in a selected area of precipitates.

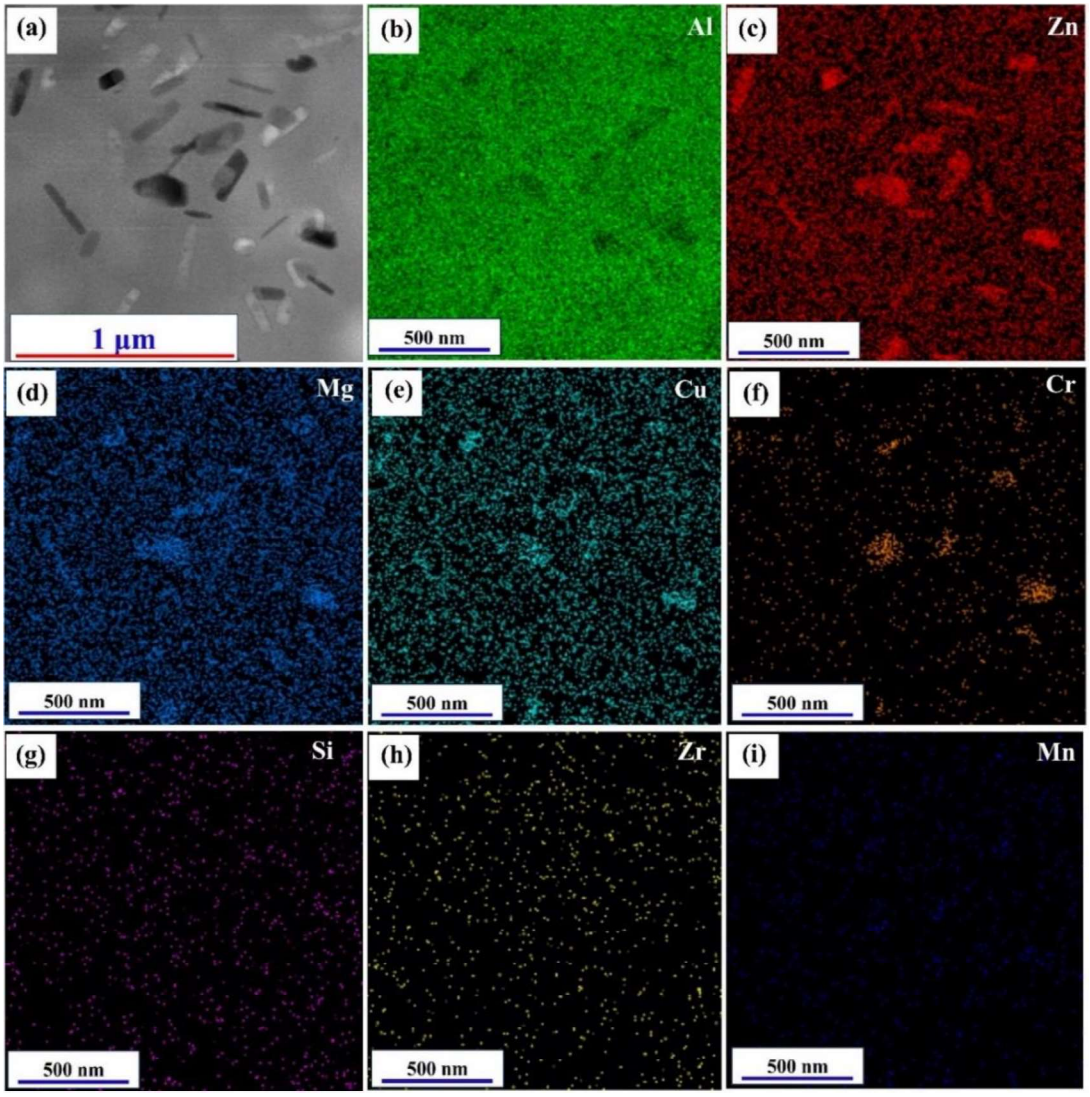

Fig. 5.21a-i STEM-EDS elemental mapping of precipitates after FSP: (a) bright-field STEM micrograph, (b) map of Al, (c) Zn, (d) Mg, (e) Cu, (f) Cr, (g) Zr, (h) Si, (i) Mn.

5.2.6 Mechanical properties

5.2.6.1 Hardness and residual stress

Fig. 5.22a displays hardness (Hv) profile, along LD (depth-wise). Three different layers, the top, middle, and bottom portions are selected for the measurement. The W-shaped hardness profiles are mainly observed in different layers. The top layer gives higher hardness followed by the middle and bottom portions. The average hardness on top of the NZ after 1pass FSP

is 155±3 Hv, which is more than the average hardness of TMAZ (147±5 Hv), HAZ (123±6 Hv) and the BM (133±4 Hv, Fig. 5.22a). The average hardness in the middle portion is 152±2 Hv for NZ followed by 144±5 Hv for TMAZ, 118±5 Hv for HAZ, and 134±4 Hv for BM. The average hardness value in the bottom portion is 147±6 Hv for NZ, followed by 141±3 Hv for the TMAZ, 117±5 Hv for HAZ, and 132±6 Hv for the BM.

The average hardness at the top of the nugget zone (NZ), after 1 pass FSP is 155±4 Hv (Fig. 5.22b). After 2pass FSP, the average hardness is 193±6 Hv (Fig. 5.22c). On the other hand, the average hardness after 3 pass FSP, is 181±5 Hv. The average hardness decreases from the NZ to the HAZ, thereafter slightly increasing in the BM region. Variations of hardness from three different layers, e.g. top, middle, and bottom potion are given in Fig. 5.22b-d

All three different zones (e.g. NZ, HAZ, and BM) result in compressive residual stress. The residual stress in NZ is -132±8 MPa which is higher than the other region (Fig. 5.22e). The residual stress in HAZ is -110±7 MPa. On the other hand, RS in the base metal region is -93±6 MPa. The residual stress in NZ after 2pass FSP is -153±7 MPa. Whereas, measured RS in NZ after 3pass FSP is -148±4 MPa. Variation of residual stress after 1 pass FSP, along (TD), is given in Fig. 5.22e. On the other hand, RS variation in NZ after multi-pass FSP is shown in Fig. 5.22f.

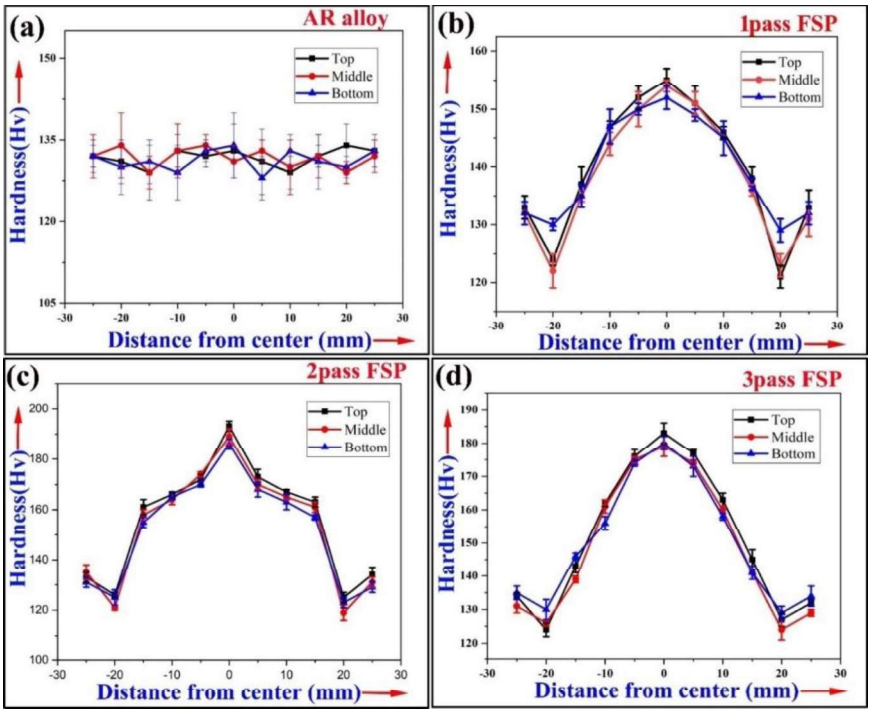

Fig. 5.22a-f Changes of hardness in AR alloy (a), after 1 pass FSP (b), after 2pass FSP (c), after 3 pass FSP (d), changes of residual stress along TD of processed alloy (f), changes of RS in from NZ after multi-pass FSP.

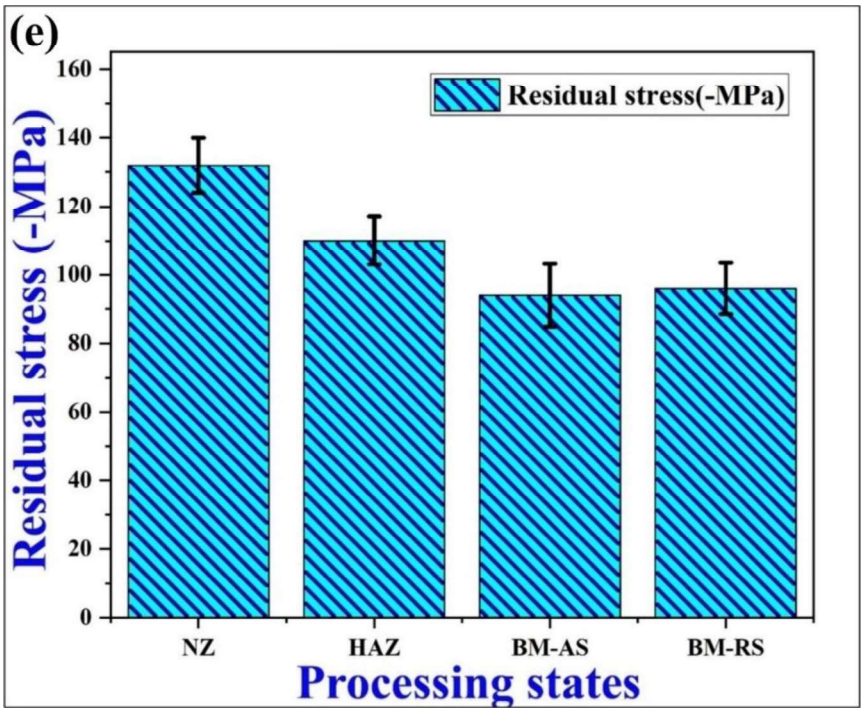

Fig. 5.22a-f Continued….

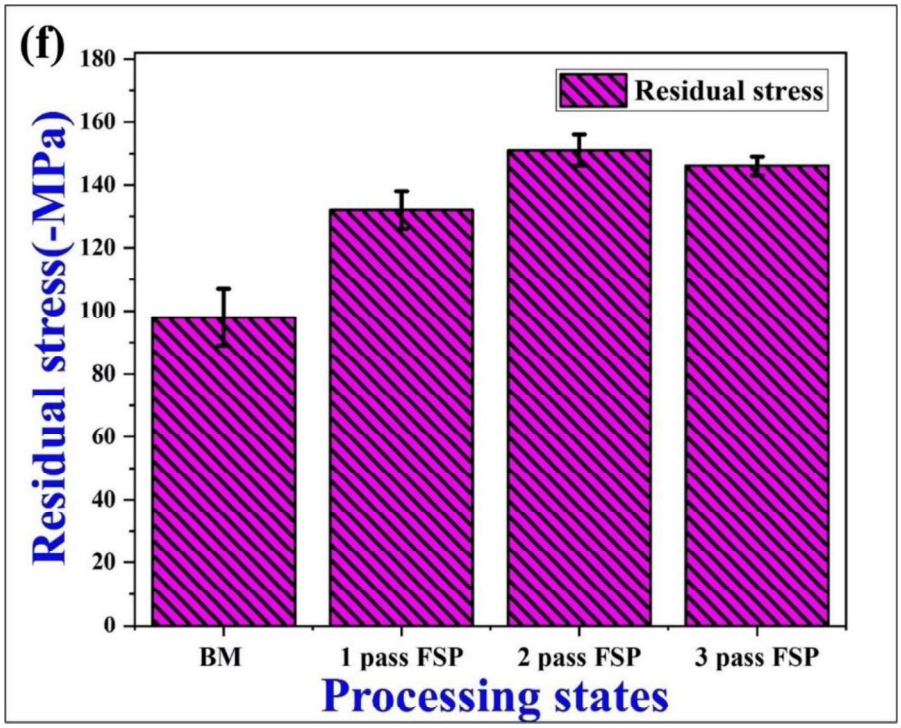

Fig. 5.22a-f Continued…….

3.5.6.2 Tensile properties

Fig. 5.23a-b displays the engineering stress vs. engineering strain plot of the AR alloy as well as after FSP. The AR alloy, at the end of the elastic limit, depicts a sharp increase of engineering stress concerning engineering strain up to UTS. After that, it decreases. After FSP, a consistent increase of engineering stress was observed concerning the engineering strain after the elastic limit, but it was lower than the AR alloy.

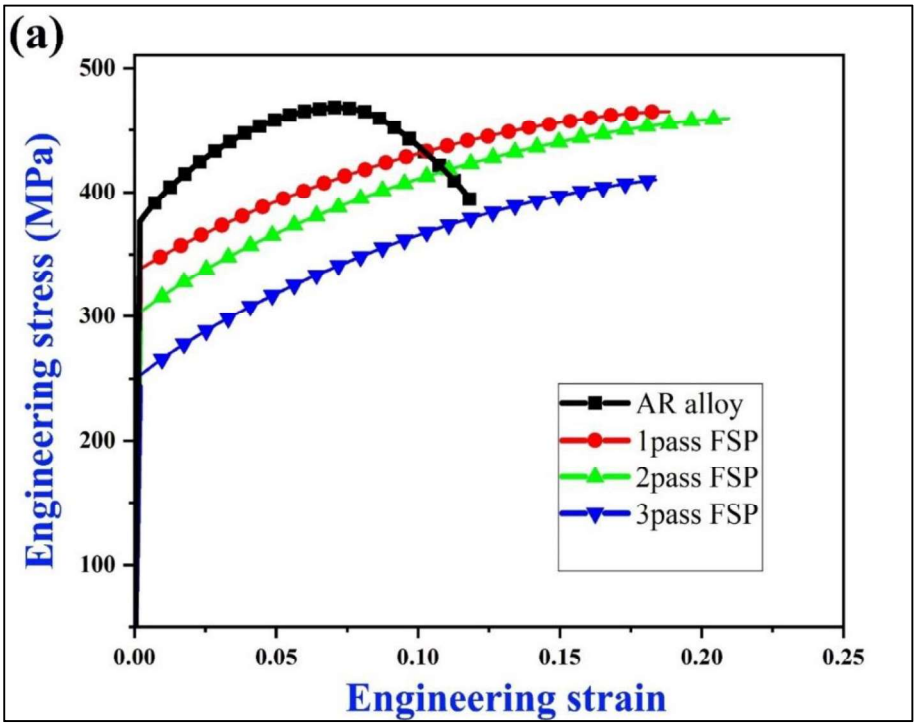

Figs. 5.23a-e. (a) Engineering stress vs. engineering strain plots for AR alloy, and after FSP, log true stress vs. log true plastic strain plot calculated from experimental data and flow curve as per Hollomon, Ludwik, Swift, Ludwigson and Voce models for (b) AR and (c) after FSP.

The tensile properties are calculated using the load versus elongation data following the standard procedures reported in the literature [252], which is given in Table 5.6.

Table 5.6 Tensile properties of the AR alloy and after multi-pass FSP

Serial No.	Specimens	YS (MPa)	UTS (MPa)	Percentage elongation (%*EL*)	UTS/YS
1	**AR alloy**	380±5	470±7	13	1.20
2	**1pass FSP**	340±3	465±8	20	1.40
3	**2 pass FSP**	303±4	460±5	23	1.51
4	**3 pass FSP**	253±6	412±4	18	1.65

The mathematical models proposed by Hollomon [170], Ludwik [171], Ludwigson [172], Swift [173], and Voce [174] were employed to obtain the strain hardening, and flow behaviors of the AR alloy, and after FSP (1pass, 2pass, and 3pass) respectively. Figs. 10b

depicts the log true stress versus log true plastic strain plot for the AR alloy. On the other hand, Figs. 5.23c-e show corresponding plots after FSP (1pass, 2pass, and 3pass respectively). The Ludwik, Ludwigson and Voce mathematical models display an upward concave shape with respect to experimental plot. On the other hand, Swift and Voce show much deviation from the experimental plot in all conditions. The AR alloy gives best fittings with the Ludwigson model (Fig. 5.23b). On the other hand, the Swift model was best fitted after FSP (Fig. 5.23c-e).

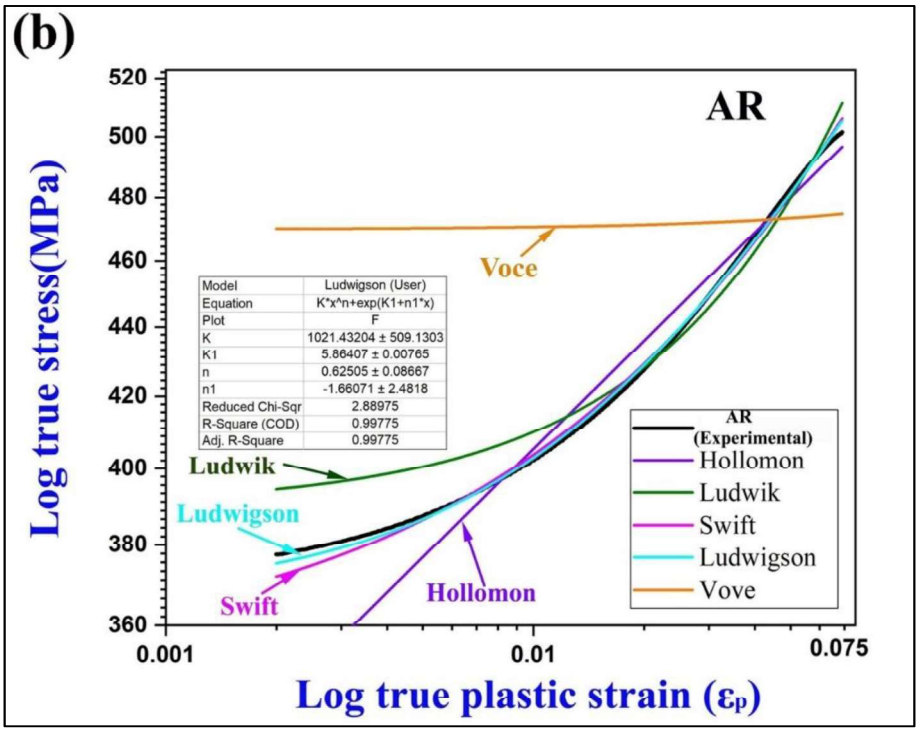

Fig. 5.23a-e Continued.....

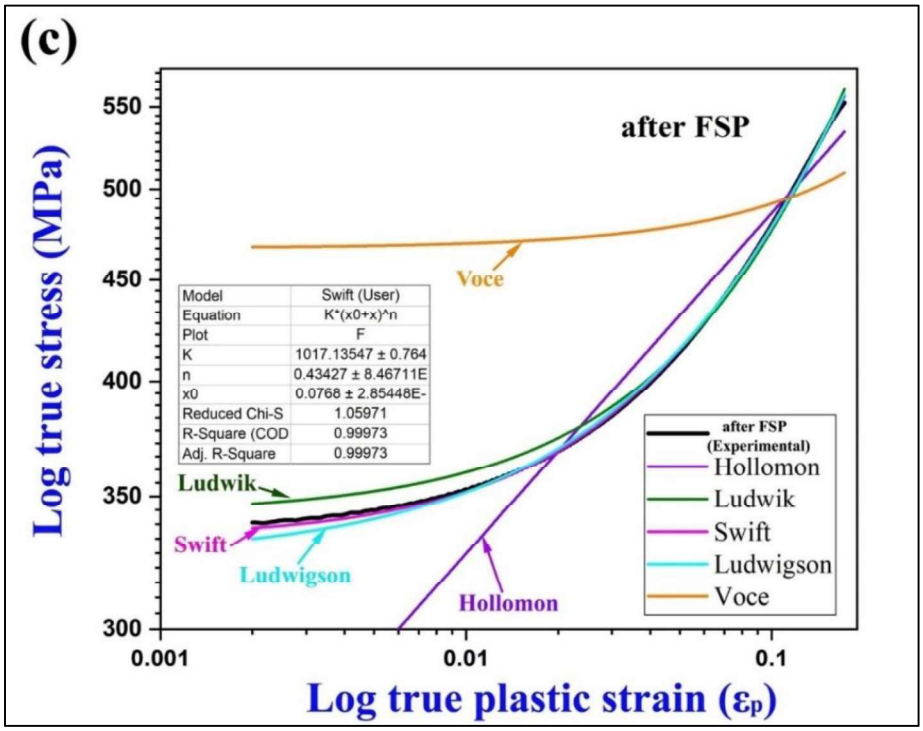

Fig. 5.23a-e Continued.....

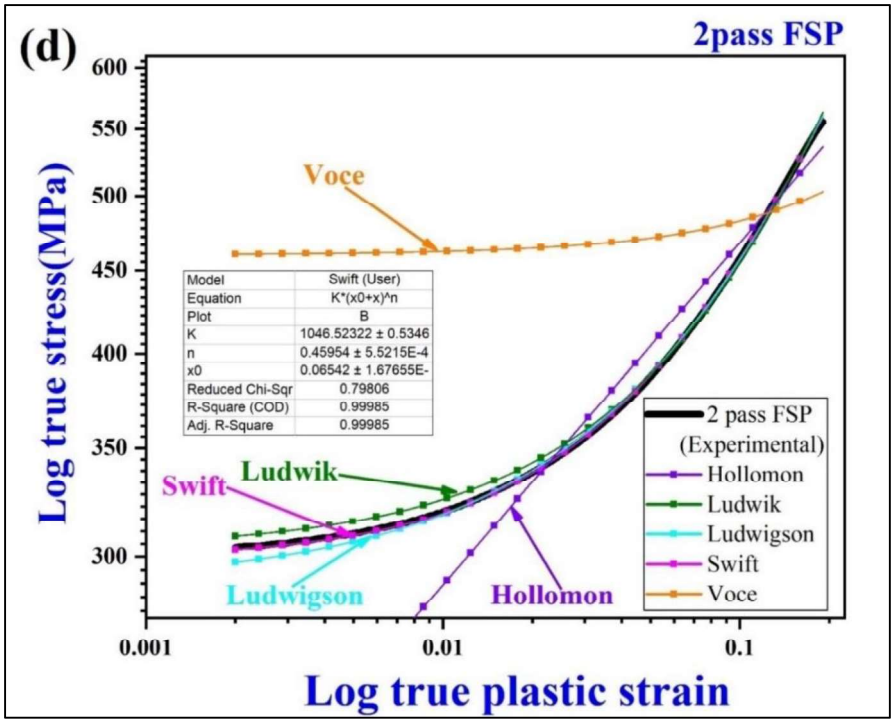

Figs. 5.23a-e Continued……

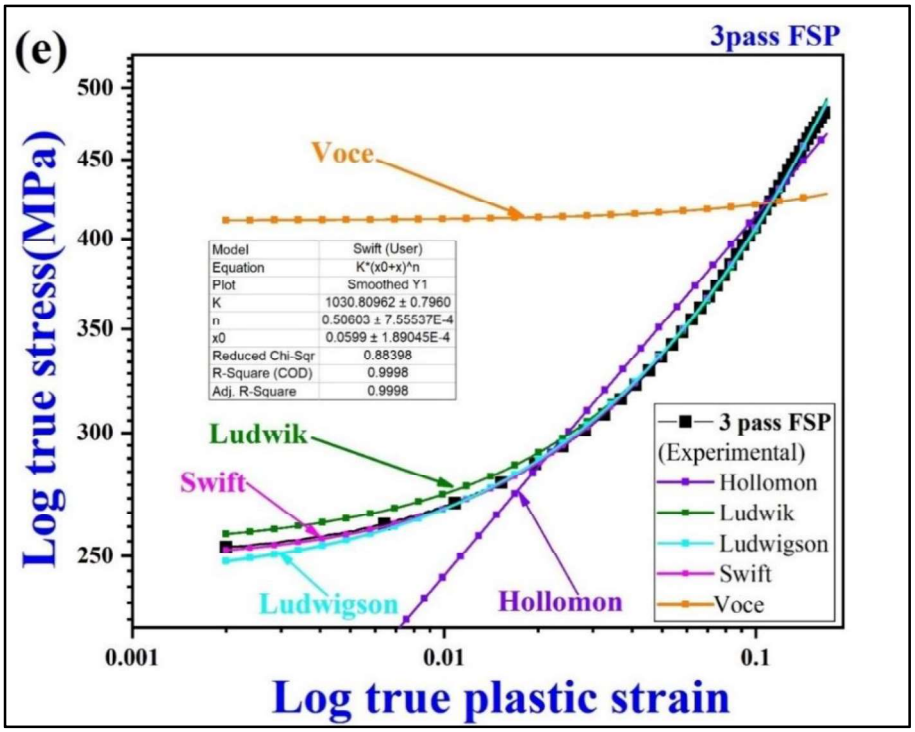

Figs. 5.23a-e Continued……

The flow parameters are determined using the best fitted mathematical models and their values are given in Table 5.7.

Table 5.7 Best fitted flow curve parameters in the AR state, and after multi-pass FSP

Alloys	**Strength co-efficient *K (MPa)***	**Hardening exponent *(n)***	**Best fittings**	***R*²**	**Flow stress K(ε_0^n), MPa**
AR	K_1=1025, K_2= 5.86	n_1= 0.62 n_2 =-1.67	$\sigma = K_1\varepsilon^{n1} + exp(K_2 + n_2 * \varepsilon)$,	0.9977	
1 pass FSP	K = 1017	n = 0.43 ε_0 = 0.0768	$\sigma = K(\varepsilon_0+\varepsilon)^n$	0.9997	337
2 pass FSP	K = 1070	n = 0.39 ε_0 = 0.025	$\sigma = K(\varepsilon_0+\varepsilon)^n$	0.9999	254
3 pass FSP	K = 1030	n = 0.50 ε_0 = 0.06	$\sigma = K(\varepsilon_0+\varepsilon)^n$	0.9998	252

Fig. 5.24a shows the hardening rate **($d\sigma/d\varepsilon$, Θ)** vs. true plastic strain **(ε_p)** plot of the AR alloy. This displays three stages of hardening behaviour. Stage I shows a sharp, concave shape of

decreasing behavior. Stage II depicts a linear decreasing trend, and its slope is less than that of Stage I. Stage III follows a linear decreasing trend, but its slope is more than Stage II. There is a range of transition true plastic strain *(ε_p)* at the end of stages I and II.

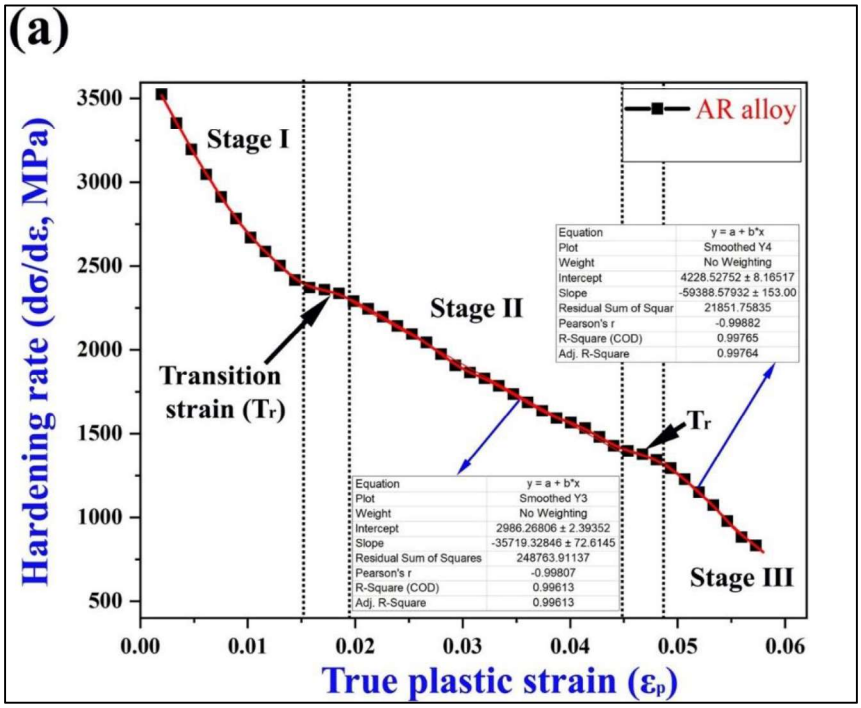

Figs. 5.24a-e hardening rate ($d\sigma/d\varepsilon$) vs. true plastic strain plot (ε_p) of AR alloy (a), ln$(d\sigma/d\varepsilon)$ vs. $ln(\varepsilon_0+\varepsilon_p)$ plot, after 1pass FSP (b), 2pass FSP (c), and 3pass FSP(d) showing three stages of hardening behavior, (e) combined ln$(d\sigma/d\varepsilon)$ *vs.* $ln(\varepsilon_0+\varepsilon_p)$ plot after FSP.

The hardening rate ($d\sigma/d\varepsilon$, Θ) is calculated at the beginning of stages I(Θ_1), II(Θ_2), and III(Θ_3). The linear decrease of hardening rate $(d\sigma/d\varepsilon, \Theta)$, respective to true plastic strain (ε_p) in stage II and stage III of AR alloys, could be best explained with the help of Kock [200], Mecking [253], and Esterin [201] (*KME*)-based dislocation model $[\Theta = \Phi_0+P\sigma]$. Here, Θ is the strain-hardening rate, and Φ_0 is the dislocation storage term. On the other hand, σ and P depict the true stress and slope of the linear portion, respectively. The slope (P) and intercept values (Φ_0) in both stages were determined by applying the linear fitting method which is given in Table 5.8.

Table 5.8 Intercept and slope of the linear portion of stages II and III, as well as Θ and ε_r at the end of all stages

Materials	Slope (n) & Intercept value		R^2	Transition true strain (ε_r)		Work hardening rates (MPa)		
	Intercept (Θ_0)	Slope (m)		ε_{r1}	ε_{r2}	Θ_1	Θ_2	Θ_3
AR-alloy	Stage II = 2986±2.3 Stage III = 4228±8.1	Stage II = -35719±72 Stage III = -59388±153	0.996 0.997	0.01518 to 0.01953	0.0485 to 0.4475	3506	2297	1322

Hardening rate ***(Θ)***, after FSP (best fitted with Swift model) is obtained after numerical differentiation of the Swift model ($\sigma = K(\varepsilon_0 + \varepsilon)^n$) concerning true plastic strain (ε_p), which can be written as $[d\sigma/d\varepsilon\ (\Theta) = Kn(\varepsilon_0+\varepsilon)^{n-1}]$. This was further converted into the logarithmic form as: $[ln(\Theta) = ln(kn)+(n-1)\ ln(\varepsilon_0+\varepsilon)]$. Here, Θ is the strain hardening rate, σ is the true stress, and ε_p is the true plastic strain. Fig. 5.24b-d shows log-log plot between the work hardening rate $(d\sigma/d\varepsilon, \Theta)$, and corrected true plastic strain $(\varepsilon_0+\varepsilon)$ after FSP (1pass, 2pass, and 3pass). The resultant plots again show three stages of hardening behavior. A slow and stagnant decreasing trend is observed in stage I. Dip and hump decreasing nature in stage II. On the other hand, drastic/ steep decreasing behavior in stage III. The plots after 2 and 3 passes of FSP display similar features of three-stage hardening curves, but the transition from stage I to state II occurs in accordance with the lower corrected true plastic strain. Stage II depicts linear decreasing behavior, but a decreasing trend is more than stage I. Stage III depicts a steep decreasing trend of hardening rate(θ) concerning corrected true plastic strain($\varepsilon_0+\varepsilon$) in both curves. The combined plots after FSP are given in Fig. 5.24e

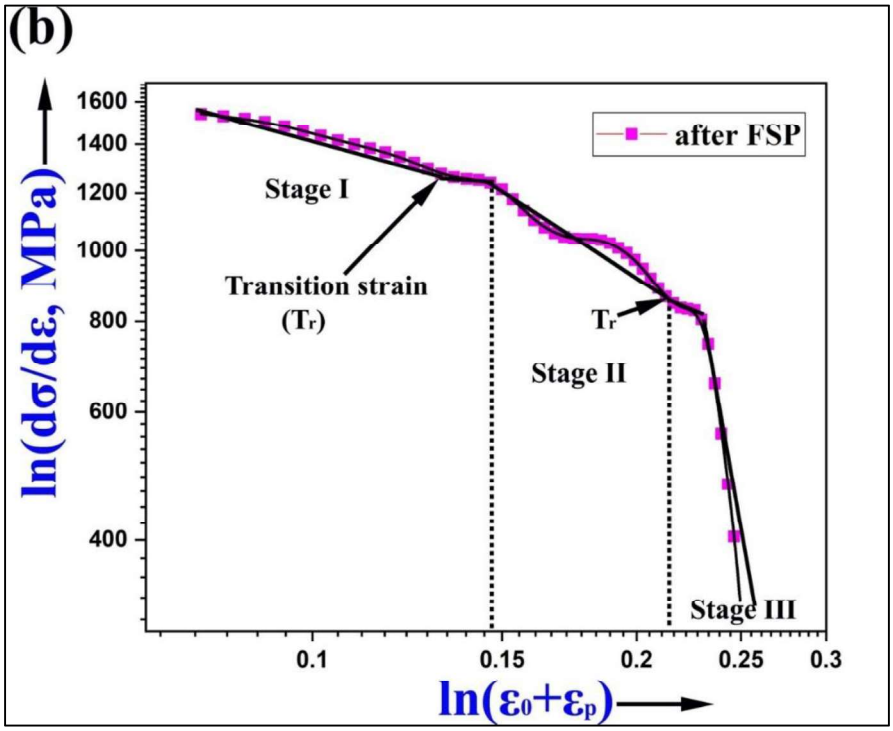

Figs. 5.24a-e Continued…….

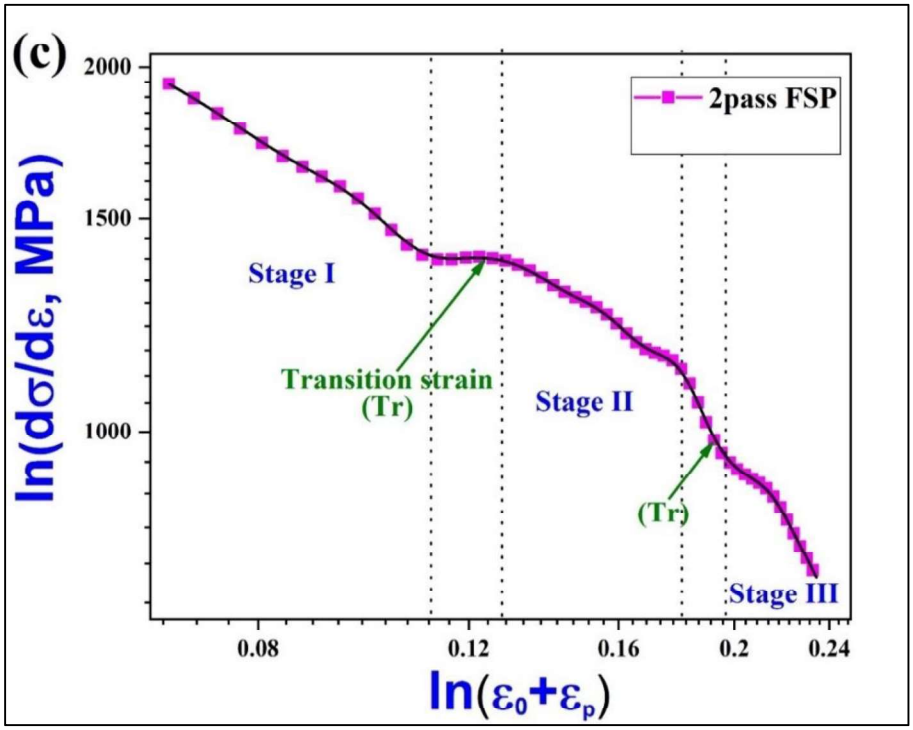

Figs. 5.24a-e Continued……

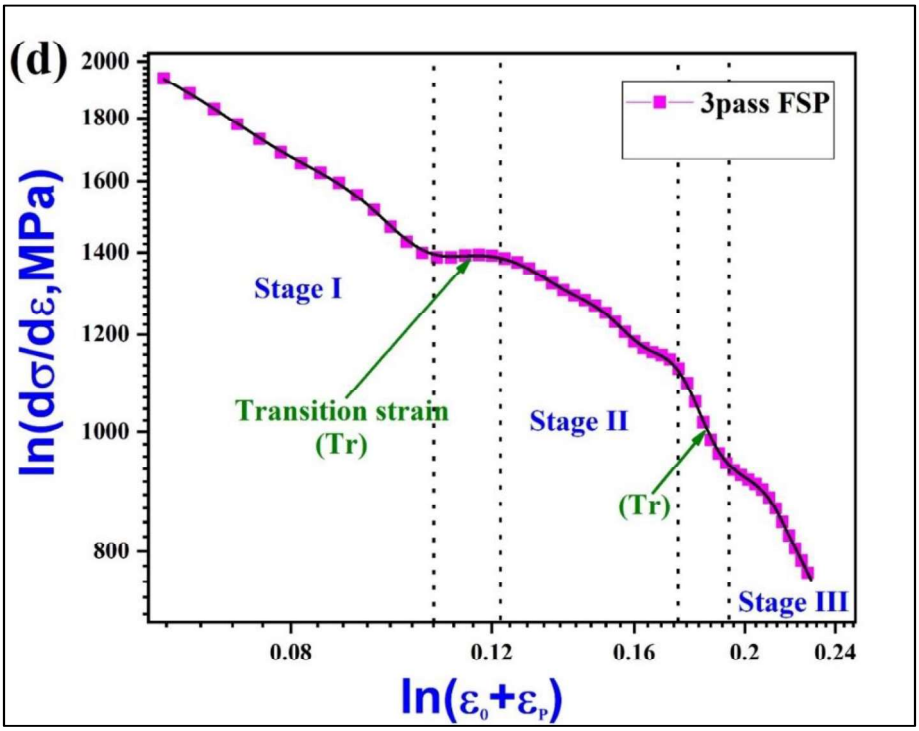

Figs. 5.24a-e Continued……

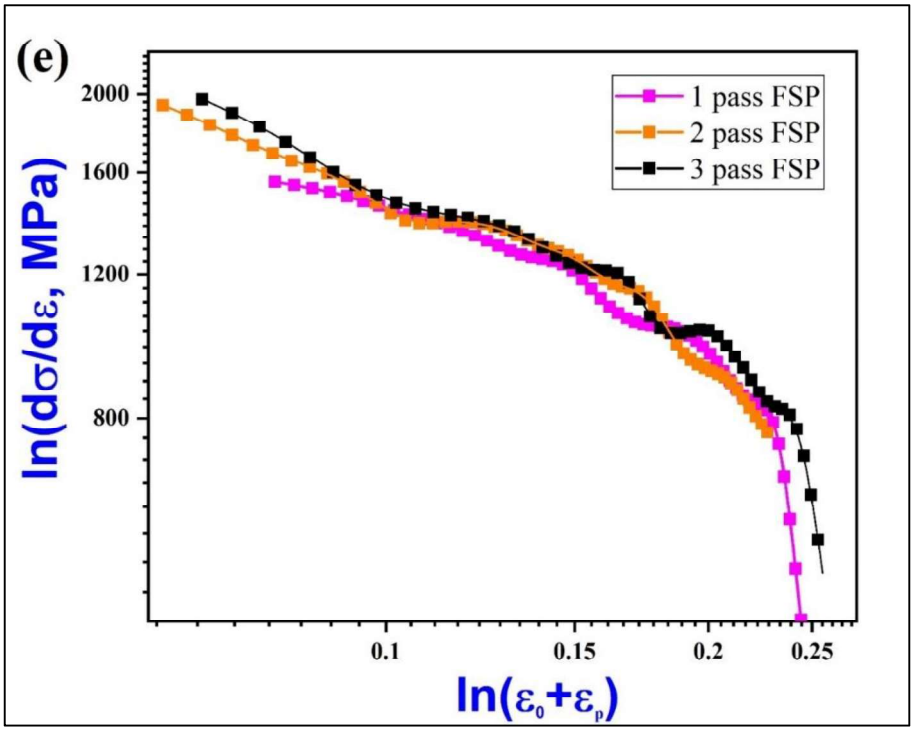

Figs. 5.24a-e Continued……

The magnitude of the slope (*n-1*), transition true plastic strain (ε_r), and hardening rate (Θ) in all three stages are determined after FSP (1 pass, 2 pass, and 3 pass respectively) using the linear fitting method. The range of corrected transition true plastic strain at the end of stages I, and II is given in Table 5.9.

Table 5.9 Magnitude of slope, transition strain, and hardening rate after FSP

Materials	**Slope** ***(n-1)***			**Transition strain** ***(ε_r)***			**Work hardening rate** **(Θ, MPa)**		
	I	II	III	ε_{r1}	ε_{r2}	ε_{r3}	Θ_1	Θ_2	Θ_3
1pass FSP	-0.38	-1.2 and -1.7	-10.17	0.1346 to 0.14	0.1714 and 0.1884	0.2163 to 0.2273	1552	1239	821
2 pass FSP	-0.65	-0.63	-1.83	0.11 to 0.12	0.18 to 0.19		1931	1385	927
3pass FSP	-0.61	-0.62	-1.84	0.10 to 0.12	0.17 to 0.19		1947	1400	894

The work hardening exponent (*n*) in each stage was determined from the magnitude of slope (n-1) between the logarithmic hardening rate versus the corrected true plastic strain curve. The hardening exponent for 1 pass FSP in stage I is 0.62 (n_1). The two different hardening exponents in stage II are -0.2 (n_2) and -0.7 (n_2) because of its dip and hump nature. The hardening exponent in stage III is -9.2 (n_3). The hardening exponent for 2 passes FSP in stage I and stage II are 0.35 and 0.37 alternatively. On the other hand, the hardening exponent in stage III is -0.83. Similarly, after 3pass FSP, the hardening exponent in stage I, and stage II are 0.39 and 0.38 respectively. Whereas, the hardening exponent in stage III is -0.84 (Table 5.9).

5.2.7 Fractography

Figs. 5.25a-b shows the fracture surface of AR alloy. The dimples and particle cracks are observed in the former (Fig. 5.25a). On the other hand, shear facets, dimples, and ruptures can be seen in the latter (Fig. 5.25b). Figs. 5.25c-d shows fracture surface after 1pass FSP. The dimples and fibrous fracture are observed in the former (Fig. 5.25c). On the other hand, particle cracks and fibrous fractures were seen in the latter (Fig. 5.25d). Figs. 5.25e-f shows fracture surface after 2pass FSP. Uniformly distributed dimples and fibrous fracture surfaces are observed in Fig. 5.25e. Whereas, fibrous fracture morphology in Fig. 5.25f. The Figs. 5.25g-h display fracture surface after 3pass FSP. The presence of dimples is observed in Fig. 5.25g but their distribution is non-uniform. Fine fibrous fracture is observed in Fig. 5.25h.

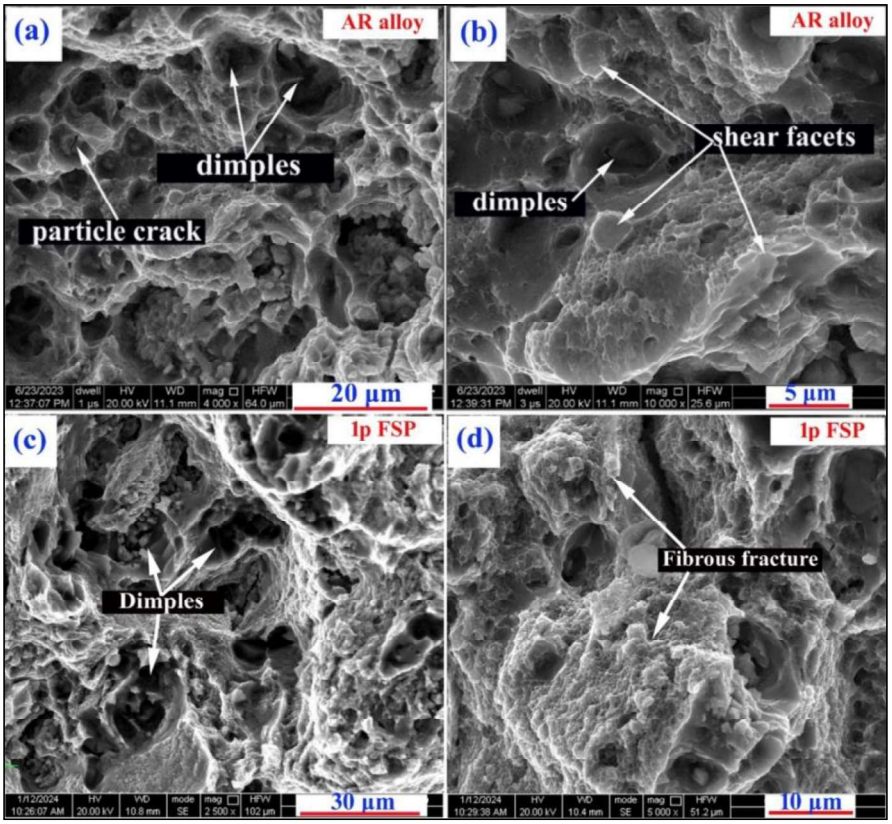

Figs. 5.25a-h Fractography of the AR alloy (a,b), 1 pass FSP (c, d), 2 pass FSP (e,f), 3pass FSP (g, h).

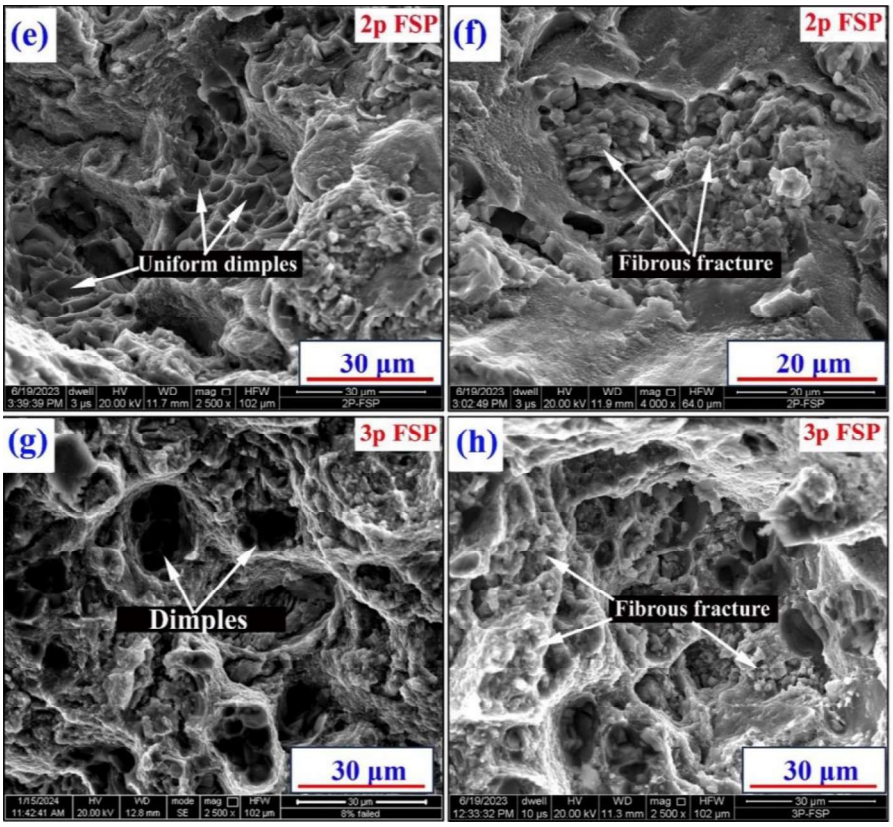

Figs. 5.25a-i Continued……

5.3 Discussion

The dark contrast in the optical micrograph of AR alloy (Fig. 5.1a) arises due to the heterophase interface of the transition (η') and equilibrium (η) precipitates. A slightly elongated but narrow TMAZ forms (Fig. 5.1b) due to the combined effect of plastic deformation and the thermal effect [107,109]. The coarse grain micro-structures in HAZ (Fig. 5.1c) emerge due to a stirring-assisted thermal environment and the absence of plastic deformation [106,109]. The very fine and equiaxed grains in NZ (Fig. 5.1c) arise due to the joint effect of the continuous dynamic re-crystallization (CDRX) and geometric dynamic re-crystallization (GDRX) [22,106]. Differences in the contrast arise due to variations in the light intensity passing through the matrix and precipitates. Matrix is a homophase interface [254], thus light passing through it gives a bright contrast. On the other hand, precipitates form a hetero-phase interface [254] due to the evolution of the semi-coherent (η') and incoherent (η) precipitates. Hence, light passing through such an interface creates a dark contrast (Fig. 5.1a). The weak crystalline peaks (Fig. 5.2a) appear due to the formation of the transition (η') and equilibrium (η) precipitates. Added to this, peaks analysis also confirms the formation of the Al_2CuMg and Al_2Cu intermetallics. The absence of a less intense crystalline peak (002) of the η after 1pass, and 2pass FSP (Fig. 5.2b-c) confirms the complete dissolution. In contrast, the evolution of the η peak after 3pass FSP displays re-precipitation. Similarly reduced intensity of the η' and η phases after FSP (1 to 3 passes) confirms the partial dissolution. No appearance of the Al_2Cu, and Al_2CuMg peaks after 2pass, and 3pass FSP (Fig. 5.2c-d) indicates the complete dissolution. The formation of new crystalline XRD peaks (113 and 024) of $Al_{23}CuFe_4$, appears due to the discontinuous type of solid-to-solid structural phase transformations [71]. The newly formed precipitates appear with different chemistry and crystal structures. The enhanced intensity of the Al2Cu peak

after 1pass FSP confirms the coarsening (Fig. 5.2b) of precipitates. Slightly right-shifted 111 peaks of α-Al support the dissolution of the phases after 1 and 2 passes of FSP (Fig. 5.2e). On the other hand, left shifting shows re-precipitation of η after 3 passes of FSP (Fig. 5.2e). Such shifting appears due to changes in the lattice parameter of α-Al.

The lattice parameter of the GP zone (4.2Å), and α-Al matrix (4.1Å) are nearly the same, with a lattice misfit of 2.8%. Therefore, the GP zone shows coherency with the α-Al. The increased lattice misfit of η' (17%) and η (25%) indicate the semi-coherent and incoherent precipitation. The DTA thermogram (Fig. 5.2f) also confirms the dissolution of the η due to more negative temperature changes respective to 523K. On the other hand, three negative peaks in NZ, respective to 523K, 663K, and 753K show the endothermic nature and support the dissolution of phases. More temperature variation in 523K confirms the complete dissolution of the η'. A less negative peak appears due to the partial dissolution (Fig. 5.2f). Precipitation in age-hardenable, 7xxx series Al-alloys are thermally activated diffusion-controlled solid-to-solid structural phase transformation of continuous type [71]. Crystal structures and composition of SSSS(α) and saturated (α) do not change as the transformations proceed, but long-range thermally activated solute transport occurs [121].

The barrier effect for nucleation of precipitates forming from the SSSS(α) is a function of the interfacial energy ($\Delta G \propto \gamma^3$) [183]. The coherent precipitate, GP zone, has low interfacial energy (0.01-0.05 J/m^2) [71,121]. Therefore, its nucleation occurs in the beginning. On the other hand, due to the high interfacial energy (0.4-1.0 J/m^2) of η phase, nucleation occurs at the end of the precipitation process. The semi-coherent η' has interfacial energy (0.1-0.3 J/m^2) between the GP zone and η. Therefore, nucleation occurs in an intermediate position [71]. Accordingly, the precipitation process of AR alloy could be described as: *SSSS(α)-GP*

zones-η'-η. The two crucial facts are observed after FSP: 1. Partial dissolution of the η' and η after 1 and 2 passes of FSP. On the other hand, re-precipitation of the η with a different chemistry but same crystal structures after 3 passes of FSP. 2. The partial dissolutions of the *η', η, Al_2CuMg,* and *Al_2Cu* (Fig. 5.2b-d) after 2 and 3 passes of FSP. 3. In contrast, the formation of new intermetallic, e.g., $Al_{23}CuFe_4$, after FSP up to 3 passes. The growth of Al_2Cu (θ) after 1 pass FSP (Fig. 5.2b). Therefore, mechanisms associated with such observations require further discussion. Dissolution of the phases is either strain-induced dissolution or may arise due to the thermal effect [175,178]. The stirring between the tool and the workpiece interface causes high strain [106,109], which produces dislocation in the matrix; thus, assisted dissolution of phases occurs. The rate of dissolution depends on the time dislocations reaching the precipitates and the nature of the interface [178]. Less time and a coherent interface could dissolve the η' immediately because the size of the η' is less and it is semi-coherent [175,178]. However, more contact time helps the dislocation-assisted growth of phases by the pipe-diffusion and dislocation-sweeping mechanisms [178,228]. The internal friction between the tool and workpiece produces heat up to 410°C in the NZ [108,178,244,255]. Such high temperature is also enough for the complete dissolution of η' (coherent), and partial dissolution of in-coherent η [178]. Therefore, thermal effect and dislocation shear are the primary responsible factors for the dissolution of η' and η after FSP in the current investigation.

Formation of the new intermetallic of $Al_{23}CuFe_4$ (Fig. 5.2b-d) up to 3 pass and re-precipitation of the η at 2θ=20°occurs which possibly arises due to separated nucleation mechanisms [68]. After the dissolution of precipitates, the fragmented particles undergo in the α-Al and remain as the solute atoms [178,187]. The dislocation introduced in the matrix during FSP collects the solute atoms and forms new phases with different chemistry and

crystal structure or different chemistry and the same crystal structure by the pipe-diffusion and dislocation sweeping mechanisms [176,178]. Such changes in the structures and chemistry after dissolution and changes in the formation of new precipitates are likely to improve the mechanical properties and the SCC performances [4]. Evolution of Goss {011} <100> texture (Fig. 5.3a-d) creates large-angle twist grain boundary to the nearby grains and makes the crack propagation torturous [256]. Hence more intensity (G, x 28R) of Goss {011} <100> texture in AR alloy (Fig. 5.3a), and sharply reduced intensity (G, x 2.4R, 1.6R and 2.1R) of Goss texture {011} <100> after FSP (Fig. 5.3b-d) gives the crack-resistant alloy [158,256], but texture-assisted crack-resistant properties will be less after FSP (1pass, 2pass, and 3pass FSP).

The sharp changes of grain size, 54±3 μm, in AR state (Fig. 5.4a) to 4.0±0.8 μm, after 1pass FSP (Fig. 5.4c), 3.5±0.6 μm, after 2pass FSP (Fig. 5.4e). On the other hand, 3.6±0.4 μm after 3 pass FSP (Fig. 5.4g), as well as those of increased HAGBFs (15% to 49%) after 1pass FSP (Fig. 5.4d), (15% to 47% after 2pass FSP (Fig. 5.4f), and (15% to 30%) after 3pass FSP (Fig.5.4h) emerges due to dynamic re-crystallization (DRx) in the top of NZ. The DRx occurs due to the combined effect of strain-induced sub-grain rotation and absorptions of the dislocation at grain boundaries in the initial stage. The GBs dominated enhanced misorientation and their further transformations into GBs in the subsequent stages [22]. Such a micro-texture evolution further helps in improving the ductility of the alloy [31].

The KAM indicates the local misorientation at the measuring point which can be used to examine the plastic strain distribution. The low KAM value (0.52) of AR alloy is due to randomly oriented coarse grain microstructures (Fig. 4g) [257,258]. In contrast, increased KAM value after 1 pass and 3 pass FSP (0.56 and 0.65) shows the increased dislocation

density. On the other hand, reduced KAM after 2pass FSP (0.45) depicts the decreasing dislocation density. This arises due to increased recovery during the dynamic recrystallization process in the NZ (Fig. 4h) [258].

The increased proportion of low CSL($\Sigma 3^n$) boundaries are corrosion and crack resistant [259]. On the other hand, this also helps maintain the fatigue resistance as well as those of obtaining the failure resistance caused by hydrogen embrittlement (HE) and stress corrosion cracking (SCC) [260,261]. Therefore, the increased low CSL boundary fractions $\Sigma 3$ =0.75 in AR state to $\Sigma 3$ =1.25 after 1pass FSP, $\Sigma 3$ =1.3 after 2pass FSP. On the other hand, $\Sigma 3$ =1.0 after 3pass FSP would likely help in obtaining the SCC, and fatigue-resistant alloy as well as those of failure resistance caused by the hydrogen embrittlement (HE).

The spherical, rod-type and plate-like precipitates (Fig. 5.9a) show the formation of the GP zone, η' and η [69,149]. The sharp DPs with d-spacing values of 1.43 Å and 2.0 Å are analyzed as the 220 and 200 spots of the α-Al (PDF#85-1327, Fig. 5.9b). On the other hand, weak DPs show the evolution of the η' and η precipitates corresponding to d-spacing values of 2.11Å, and 1.91Å alternatively (Fig. 5.9b) (PDF#77-1177). The mathematical relationship proposed by Nabarro [120] mainly decides the shape and morphologies of precipitates on account of the elastically soft direction for the nucleation and growth of precipitates. Accordingly, the precipitates with rod-type precipitates are recognized as the η', and plate-like precipitate morphologies are denoted as the η precipitates (Fig. 5c). Such analyses were also made on the account of the precipitates morphologies and the SAEDPs~ reported in the literature [47,48,90,149,262]. The sharp superlattice DPs with *4-fold* symmetry (Fig. 5.9b) are from 200 of the *α*-Al. Moreover, weak and ordered DPs with *4-fold* symmetry/ satellite spots ~ (Fig. 5b) are from the η' and η precipitates [47]. The evolution of the forest

dislocation as observed in the WBDF-TEM micrograph (Fig. 5.10g) is a characteristic feature of the low hardening [93,95]. On the other hand, DDWs observed in Fig. 5.10e and h, are characteristic features of the high hardening [95].

The parallel array of dislocation, and dislocation peening (Figs. 5.11a, c,d) on top of the NZ, after 1pass FSP, arises due to the combined effect of the thermal environment as well as those of the plastic deformation. Such structural evolution is part of the recovery process which later produces the dynamic re-crystallized grain structures. During the recovery process dislocation re-arrangement mainly occurs on account of the variation of strain and temperature during processing of the alloys. The parallel array of dislocation structures, and dislocation network (hexagonal and tetragonal shape, Fig. 5.12a,c,d) formation in the middle portion are characteristic features of the medium to high hardening [95,96], which may cause high hardening to the alloy by activation of the multiple slip systems [90,126,180].

Formation of the sub-grain microstructure as well as those of dislocation cell structures in the bottom portion are characteristic features of the medium to high hardening (Fig. 5.13a,c) [96,193]. Such structural evolution helps in activating the multiple slip systems thus producing medium to high hardening in the alloys [95]. The diffracted g-vector (200) of α-Al, in 2-beam condition on the top portion (Fig. 5.11b), a 3-beam condition in the middle (Fig. 5.12b), and the bottom (Fig. 5.15b, d) portion also support the dislocation structure evolution. The structural evolution from top to bottom (Fig. 5.11to Fig. 5.13) also shows dislocation re-arrangement as the parallel array of dislocation in the top to network structure formation in the middle. On the other hand, sub-grain or dislocation cell-type structures are in the bottom portion of the processed zone [96]. Such structural variation mainly arises due to changes in temperature from the top to the bottom portion of NZ. On the other hand, there is a variation of the strain from the advancing side (AS) to the re-treating side [14]. The

dislocation re-arrangement is a characteristic features of the recovery process [141], which support the structural evolution in NZ after 1pass FSP. The absence of the spherical morphologies and reduction in the number density of η' precipitates show the complete and the partial dissolution of phases in bright, and dark field TEM micrograph (Figs. 5.15a-c), as well as those of STEM micrograph after 2pass FSP (Fig. 5.17e, f). Similarly, the appearance of the spherical morphology in bright and dark field TEM micrographs (Fig. 5.16a-c), as well as those in STEM micrographs (Fig. 5.17g-h) after 3pass FSP, also support the re-precipitation of the ηas well as decreased number density of η' show partial dissolutions. The area spectrum and elemental mapping of precipitates in AR state (Fig. 5.18a-b and Fig. 5.19a-i) and after FSP (Fig.5.20a-b and Fig.5.21a-i) also confirm changes in the chemistry and size of precipitates after FSP.

Enhanced hardness value in NZ after FSP (Figs. 5.22b,c,d) arises due to grain refinement and increased dislocation density [263]. On the other hand, hardness variation from top to bottom is due to the micro-structural gradient produced due to variations in temperature and strain while processing. The reduced hardness in HAZ (Figs. 5.22b-d) is due to thermally assisted grain coarsening (Fig. 9c). Coarse grain minimizes the intensity of the strain field thus reducing the hardness [22,264]. The relatively higher residual stress (-132±8 MPa for 1pass FSP, -153±4 MPa for 2pass FSP, and -148±MPa for 3pass FSP, Fig. 5.22F) in NZ concerning HAZ (-126±4 MPa) and BM (-98±5 MPa) of 1pass FSP (Fig. 5.22e) arises due to DRx assisted very fine grain microstructure evolution. The relatively less compressive residual stress in HAZ is due to thermally assisted coarse grain formation. The compressive residual as obtained in different regions of the processed zones is likely to help in improving the resistant property thereby the mechanical performances, e.g. fatigue and stress corrosion cracking (SCC) [15].

The sharp increase in engineering stress respective to engineering strain after elastic limit and up to UTS of AR alloy is due to the interaction between matrix and precipitates which causes a hardening effect (Fig. 5.23a). The slow but continuously increasing behavior after the elastic limit after FSP (1 pass, 2 pass) arises due to the dissolution of the η' and η (Fig. 5.23a). Formation of a new intermetallic $Al_{23}CuFe_4$, after FSP, and chemistry changes results in the continuously increasing engineering stress vs. engineering strain curve. High UTS (467±3 MPa, Table 5.4) after FSP, in comparison to AR alloy, emerges due to uniformly distributed fine grains in NZ [22,265–267]. The high UTS/YS ratio, after multipass FSP (Table 5.4), is due to enhanced UTS without significant changes in the YS. After FSP, complete dissolution of the GP zone as well as partial dissolution of the η' and decreased YS with minor changes in UTS produces a high UTS/ YS ratio which is desirable for the aviation industry before applying them in structural engineering applications. The total elongation increases after FSP due to the dissolution of the hardening precipitates. On the other hand, total elongation after 3 passes was slightly less than the 2 pass, and 1 pass FSP, due to re-precipitation of the GP zone (Fig. 5.23a). Various mathematical relationships were proposed by Ludwik [171], Ludwigson [172], Hollomon [170], Swift [173], and Voce [174] to study the plastic flow behaviors of the alloy. One of the best-fitted Ludwigson relationships $(\sigma = K_1\varepsilon^{n1} + exp\ (K_2 + n_2 * \varepsilon))$ of AR alloy (Fig. 5.23b) illustrates the two-slope deformation characteristics and indicates the evolution of two different deformation mechanisms during the plastic deformation. Many investigators reported different mechanisms associated with the two-slope deformation characteristics. For instance, Mehta et al. [180], reported texture and dislocation assisted two-slope deformation in the Ni-based superalloys. Banumathy et al. [195], investigated phase transformations dominated two-slope deformation behaviors. The precise mechanisms causing the two-slope deformation in AR 7075 Al alloy require

further discussion. Some literature [90,126,193] gives the structural features responsible for such a two-slope deformation. Dislocation loops and forest dislocation-type structures [90,126,193] are related to the low-strain regimes. Moreover, the complex dislocation structures, e.g., dislocation tangles (D.T.), dense dislocation walls (DDWs~), dislocation cell (D-cell), and an array of dislocation structures [95,194,268,269] are signatures of the higher strain regimes. This kind of structural evolution very strongly hinders the motion of the mobile dislocation by activating the multiple slip systems [126,268] and causes high hardening/pre-strain in the alloy system. Hence, the cause of two slope deformation characteristics in AR alloy requires further discussion. Apart from the evolution of metastable (η') and equilibrium (η) precipitates, the dislocation forest, and the DDWs are also noticed in the AR alloy (Figs. 5.10e, h). The forest dislocation (Fig. 5.10g) causes less barrier effect for dislocation motion, thus resulting in less strain hardening (n_2=-1.68, Table 6) and attributed to the structural evolution in low strain regime. On the other hand, DDWs (Fig. 5.10e, h strongly stops the dislocation motion or traps the dislocation inside the dense dislocation walls, thus providing a high-strain hardening effect (n_1=0.62, Table 5.6) and attributed to the structural evolution in a high-strain regime. The intense (x 28R) Goss {011} <100> texture in the AR state (Fig. 5.3a) may be another possible cause of high hardening at higher sites.

The transformation of the flow behaviors from the Ludwigson in the AR alloy to Swift after FSP (1 pass, 2 pass, and 3 pass) possibly arises due to the dissolution of the GP zone and those of the gradients of the dislocation structure. The dislocation forest, low and high density of the parallel but wavy array of dislocation structures (Figs. 5.11a, c, d) may cause a pre-strain effect in the top portion and the grain refinement. The evolution of the low and high density of the parallel array of dislocation structures with the hexagonal and rectangular

network (Figs. 5.12a, c, d) may cause a strain effect in the middle portion. The less-dense structure causes less pre-strain, whereas high-density structural evolution may produce a more pre-strain effect. Such variations in the dislocation structure evolution and their re-arrangement arise due to the combined effect of the temperature and strain, which was well investigated in the literature for cubic close-packed metallic systems [30]. Apart from the dislocation structure (Fig.5.11 to Fig. 5.13) evolution, Intensity of Goss {011} <100> texture also changes sharply from x28 R in AR state (Fig. 5.3a) to x 2.5 R for 1pass FSP (Fig. 5.3b), x 1.6R after 2pass FSP (Fig. 5.3c). On the other hand, x 2.1 R after 3pass FSP (Fig. 5.3d), which may be another possible cause of changes in flow behaviors from Ludwigson in AR alloy to the Swift after FSP. Added to this, the structural phase transformations, for instance, dissolution of η', η and Al_2CuMg, and formation of new $Al_{23}CuFe_4$ intermetallic (Fig. 5.2b-c) may be another cause of Swift flow behavior, thus producing pre-strain in materials.

The sharp decrease of hardening rate $(d\sigma/d\varepsilon)$ concerning true plastic strain (ε_p) in stage-I of AR Alloy (Fig. 5.24a) arises due to dislocation structure evolution [25,180]. It indicates the single active slip system, also known as the elastoplastic transition stage. Dislocation loops and forest dislocation are the possible microstructures in this region [95]. The slow but linear decreasing of hardening rate $(d\sigma/d\varepsilon)$ respective to true plastic strain (ε_p) in Stage-II (Figs. 5.24a) emerges due to DDWs/ cellular dislocation assisted multiple active slip systems. The tangled dislocation, Taylor-lattices, and slip-band are the typical microstructure evolution in this stage [95].

The sharp but linear decreasing curve between hardening rate $(d\sigma/d\varepsilon)$ vs. true plastic strain (ε_p) in Stage III arises due to the recovery process. The dislocation re-arranges in the cellular structure form is the characteristic feature in this stage [93,95,96]. The linear relationship in

Stage II and Stage III of AR alloy could be best explained with the help of Kock, Mecking, and Esterin (KME) [200,201] based dislocation model, [$d\sigma/d\varepsilon\ (\Phi) = \Phi_0 + P\sigma$], where Φ is the work hardening rate, σ is the true stress, P is slope of the linear portion, and the intercept Φ_0 is the dislocation storage term. The more negative slope (P=-59388±150, Table 7) value in stage III, in comparison to stage II (-35719), arises due to high recovery in stage III as compared to stage II. Whereas the high intercept value (Φ0=4228±8, Table 7) in stage III shows the high dislocation storage capacity in comparison to stage II (Φ0=2986±8,) which supports the more recovery in stage III. After FSP, the three stages of hardening rate $(d\sigma/d\varepsilon)$ respective to corrected true plastic $(\varepsilon_0+\varepsilon)$ also arise due to different dislocation structure evolution. The slope in sage I is less, showing the easy glide due to the high content of mobile dislocation in the initial stage of plastic deformation [25,270]. The single slip system is generally active in this stage, and the dislocation loops, forest dislocation, and recovered microstructures are also characteristic features of this stage [92]. The slope in stage II (-1.2, Table 5.8) is more than that of stage I (-0.38), which arises due to a reduction in hardening rate $(d\sigma/d\varepsilon)$ because multiple active slip systems are active in this region [92,270].

The wavy array of dislocation structures and dislocation network (polygons: hexagonal or tetragonal dislocation network, Fig. 5.11a, c,d) are the possible structure evolution in this stage [92,95,96]. The slope in stage III (-10.17) sharply increased as compared to stage II (-1.2) and stage I (-0.38) due to significantly less or absence of strain hardening and increased dynamic recovery assisted by the dislocation. The cellular dislocation structure, or the recovered microstructures, are the possible features in this stage [92,96].

The dimples, particle-crack, and shear facets are observed in the fractography of AR alloy (Fig. 5.25a, b), indicating the mixed mode of the ductile and the brittle failures [90,255]. The

dimple ruptures (Fig. 5.25 b) show the coalescence of dimples during plastic deformation and depict the ductile fracture mode [90]. After FSP (1 pass to 2 passes, Fig. 5.25c, d and Fig. 5.25e, f), fibrous fracture surface and increased dimple size cause the ductile failure. Such fracture surface again supports the enhanced ductility/elongation after 1 pass, and 2 pass FSP [255]. The high UTS after FSP arises due to uniformly distributed solutes or fibrous structures, which may sustain more loading during tensile plastic deformation. The fibrous fracture arises due to dynamic recrystallization-assisted fine and equi-axed grain evolution [255].

5.4 Conclusions

1. After FSP, the η' and η precipitates are partially dissolved. However, a new intermetallic of $Al_{23}CuFe_4$ is separately nucleated. The phase transformation of a new phase is thermally activated solid-to-solid structural phase transformation of the discontinuous type.

2. Gradients of the dislocation structure evolution are due to temperature variations from the top to bottom and strain changes from the advancing side to the re-treating side.

3. Dislocation re-arrangement occurs from the top to bottom, e.g., recovered microstructure and dislocation pile up in boundaries at the top. Network structure formation is in the middle, whereas dislocation cell type of structural evolution is at the bottom.

3. Increased compressive residual stress and grain refinement after FSP will likely improve the mechanical properties (fatigue) and stress corrosion cracking (SCC) resistance.

4. Ludwigson flow behaviour of AR alloys arises due to forest dislocation and DDWs. The intense Goss {011}<100> texture is another possible cause.

5. Grain refinement, increased high-angle grain boundary fraction, and compressive residual stress enhance hardness, strength, and ductility and indicate the dynamic recrystallization after FSP

6. Hardness variation across the depth is due to the gradient of structural evolution and dislocation density.

7. Evolution of the less intense Goss {011} <100> texture and formation of new phases and dislocation structures are major factors for the Swift fitted flow behaviors.

8. Fractography of as-received specimens displays mixed modes of ductile and brittle failures. Fine and uniformly distributed dimples, grain boundary sliding, grain elongation, and fibrous morphologies are noticed after FSP.